Applied Thermal Engineering 190 (2021) 116793

Contents lists available at ScienceDirect

Applied Thermal Engineering

journal homepage: www.elsevier.com/locate/apthermeng

Study of paraffin-based composite-phase change materials for a shell and tube energy storage system: A mesh adaptation approach

Ali Veismoradi [a], Mohammad Ghalambaz [b,c,*], Hassan Shirivand [d], Ahmad Hajjar [e], Abdulmajeed Mohamad [f], Mikhail Sheremet [g], Ali Chamkha [h,i], Obai Younis [j,k]

[a] Chemical Engineering Department, Ferdowsi University, Mashhad, Iran
[b] Metamaterials for Mechanical, Biomechanical and Multiphysical Applications Research Group, Ton Duc Thang University, Ho Chi Minh City, Vietnam
[c] Faculty of Applied Sciences, Ton Duc Thang University, Ho Chi Minh City, Vietnam
[d] Faculty of Mechanical and Energy Engineering, Shahid Beheshti University, Tehran, Iran
[e] ECAM Lyon, LabECAM, Université de Lyon, Lyon, France
[f] Department of Mechanical and Manufacturing Engineering, Schulich School of Engineering, CEERE, The University of Calgary, Calgary, AB T2N1N4, Canada
[g] Laboratory on Convective Heat and Mass Transfer, Tomsk State University, Tomsk, Russia
[h] Faculty of Engineering, Kuwait College of Science and Technology, Doha District, Kuwait
[i] Center of Excellence in Desalination Technology, King Abdulaziz University, P.O. Box 80200, Jeddah 21589, Saudi Arabia
[j] Department of Mechanical Engineering, College of Engineering at Wadi Addwaser, Prince Sattam Bin Abdulaziz University, Saudi Arabia
[k] Department of Mechanical Engineering, Faculty of Engineering, University of Khartoum, Sudan

ARTICLE INFO

Keywords:
Phase change material
Metal foam
Shell and tube energy storage
Natural convection
Numerical simulation
Adapted mesh

ABSTRACT

Energy storage systems based on phase change materials are very innovative and useful in different engineering applications. The present study deals with numerical simulation of energy transport performance in a shell and tube energy storage system, including the paraffin wax or copper foam insertion with paraffin wax. The mathematical description of the considered problem consists of the basic equations grounded on the conservation laws with appropriate initial and boundary conditions. These equations were solved by the finite element method. The developed code was verified using the mesh sensitivity analysis and numerical data of other authors. Effects of the porosity, Rayleigh number, melting temperature, heat pipes location on melting flow structures and energy transport, and Nusselt number and melting volume fraction were scrutinized for charging and discharging modes. It was found that in the case of porous metal foam, the phase change intensity increases for the mentioned two regimes in comparison with pure paraffin wax. The vertical placement of the heating tubes results in the best charging time.

1. Introduction

Phase change materials are very innovative and useful media that can be employed in various industrial and engineering applications such as air conditioning systems [1,2], thermal management systems [3], pavement thermal management [4], and buildings [5].

Many scientists performed experimental and theoretical analyses of phase change material behavior within different engineering systems. Gurel [6] numerically studied the phase change material melting within the plate heat exchanger by the finite volume method. The author investigated the phase change material influences, heat transfer inlet temperature, metal plate thicknesses, and system geometry using the Fluent software. The author revealed that n-octadecane is characterized by low charging time in comparison with RT-35. Alizadeh et al. [7] computationally investigated an opportunity to employ fins and nanoparticles to optimize triplex-tube heat energy storage based on PCM (phase change material). The discharging mode was simulated using the FlexPDE software. The Authors showed that employing the V-shaped fins is more effective than an increment of the fins thickness.

Moreover, an intensification of the solidification process can be reached with the addition of carbon nanotubes to water. An impact of organic PCM on heat storage system efficiency was studied computationally and experimentally by Koukou et al. [8]. Thermocouples were

* Corresponding author at: Ton Duc Thang University, Ho Chi Minh City, Vietnam.
E-mail addresses: ali.veismoradi@mail.um.ac.ir (A. Veismoradi), mohammad.ghalambaz@tdtu.edu.vn (M. Ghalambaz), hassan.shirivand@yahoo.com (H. Shirivand), ahmad.hajjar@ecam.fr (A. Hajjar), mohamad@ucalgary.ca (A. Mohamad), sheremet@math.tsu.ru (M. Sheremet), a.chamkha@kcst.edu.kw (A. Chamkha), oubeytaha@hotmail.com (O. Younis).

https://doi.org/10.1016/j.applthermaleng.2021.116793
Received 27 August 2020; Received in revised form 10 February 2021; Accepted 22 February 2021
Available online 26 February 2021

Nomenclature

Latin symbols

$q_0^{''}$	the pipe surface heat flux (W/m^2)
A_{mush}	a large value for mushy term (kg/m^3 s)
C_p	heat capacity per unit mass (J/(K·kg))
D	tube shell diameter (m)
d	heat-pipe diameter (m)
Da	Darcy number (κ/H^2)
e	a minor value for mushy term
Ec	non-dimensional distance between the center of the heated tubes
g	gravitational acceleration (m/s^2)
H	tube shell scale
h_{sf}	the melting latent-heat (J/kg)
k	coefficient of thermal conductivity (W/(m K))
L	the straight heat pipe length
l	the distance between the center of the heated tubes
MVF	the scaled molten volume portion
n	the normal vector to a surface (m)
p	the pressure (Pa)
P	the scaled pressure
Pr	Prandtl number, $\nu/\alpha_{m,l}$
Q“	the scaled heat flux
Ra	Rayleigh number, $(g\beta_l \Delta T H^3)/(\nu_l \alpha_{m,l})$
s	the enthalpy-porosity's source (mushy source term)
S	the scaled mushy source term
Ste	Stefan number, $((\rho C_p)_{m,l}\ \Delta T)/(\rho_l h_{sf,m})$
t	the time (s)
T	the temperature (K)
u, v	the x and y velocity components (m/s)
U, V	the scaled X and Y velocity components
x, y	the x and y -coordinates (m)
X, Y	the dimensionless X and Y –directions

Greek symbols

ϕ	the melt volume fraction
α	the thermal diffusivity (m^2/s)
β	the volumetric thermal expansion (1/K)
γ	basis variables for finite element method
$\delta\,\theta$	The scaled temperature phase change interval
δT	the phase change interval (K)
ΔT	the temperature scale (K), $H \times q$“$_o/k_{m,l}$
ε	the porosity of the metal foam
θ	non-dimensional temperature
κ	the metal foam's permeability (m^2)
μ	the dynamic viscosity (kg/(m·s))
ν	the kinematic viscosity (m^2/s)
ξ	pore density (PPI)
ρ	density (kg/m^3)
τ	the non-dimensional time

Subscripts

a	average
adapt	adaptation
bottom	the bottom heated tube
c	cold area, tube distance
f	melting
h	hot area
k	dummy index
l	liquid/molten PCM
m	effective of the PCM and porous matrix, dummy index
s	solid PCM
top	top heated tube

used for the temperature measurement within the considered system, while charging and discharging regimes were observed naturally. The Fluent software performed the computational investigation. The authors revealed that organic PCMs illustrate a super cooling influence during the discharging mode during the analysis. Park et al. [9] experimentally studied an opportunity to improve the external waste energy utilization system employing PCM in order to augment engine efficiency. It was ascertained that stearic acid could be considered as a good PCM for the considered purpose.

Tiari et al. [10] examined the computationally discharging process of finned energy storage filled with PCM. Commercial Fluent software was used for analysis. The authors revealed that the number and length of fins accelerate the discharging regime of PCM. Faegh and Shafii [11] performed an experimental investigation of PCM usage for solar stills' energy storage. Authors showed that using the paraffin wax and heat pipes allows continuing the desalination process a few hours at night. He et al. [11] numerically and experimentally scrutinized heat transfer within aluminum tubes filled with paraffin wax. Comsol software was employed for numerical analysis. Some interesting and useful results for PCM usage in solar collectors can be found in [12,13].

The recent investigations indicate that nanoparticles' addition to a base fluid and synthesis of a nanofluid could improve the thermal conductivity of the working fluid and improve heat transfer. In this regard, alumina nanoparticles [14,15], silicon carbide [16], and other nanoparticles were used. Hence, some researchers utilized a combination of nanoparticles and PCMs [17] to improve heat transfer. The encapsulation of PCMs was another approach to improve their thermal performance [18–20].

In the optimization of cooling systems for the heat-generating elements, PCM utilization can be beneficial [21–25]. Bondareva and Sheremet [21,22] and Bondareva et al. [23–25] studied the effects of PCM load and finned heat sink on energy dissipation from the heat-generating element. The authors studied the influence of the fins parameters, heat generation, nature of the local element, phase change materials, and nanoparticle inclusion within PCM on the charging and discharging processes and energy release efficiency.

A comprehensive investigation of phase change processes and energy storage of phase change materials under various impacts, including porous media [26], solid inserted fins [27], nanoparticles [28] and metal foams [29], geometrical aspects [30,31], or PCM cases [32] have been investigated.

The literature review [26,29,31–37] shows that a combination of phase change materials with metal-foam porous media can essentially intensify the phase change processes by improving the effective thermal conductivity of composite PCM-foam [26,29]. However, it could also suppress natural convection flows. Moreover, the presence of metal foam could fundamentally affect the geometrical design of an energy storage unit. Therefore, the present study's objective is a theoretical investigation of the impact of tube arrangement and orientations on the charging and discharging time of a shell and tube thermal energy storage unit filled with copper foam and saturated with phase change material.

2. Mathematical model

The phase change heat transfer behavior in a heat exchanger energy storage system is investigated considering two configurations, including paraffin wax or paraffin wax embeded in an open-cell copper metal foam. The thermal efficiency and the heat capacity of the PCM-heat exchanger are addressed. The model of the heat exchanger is depicted in Fig. 1. The heat exchanger consists of a shell and a tube containing a

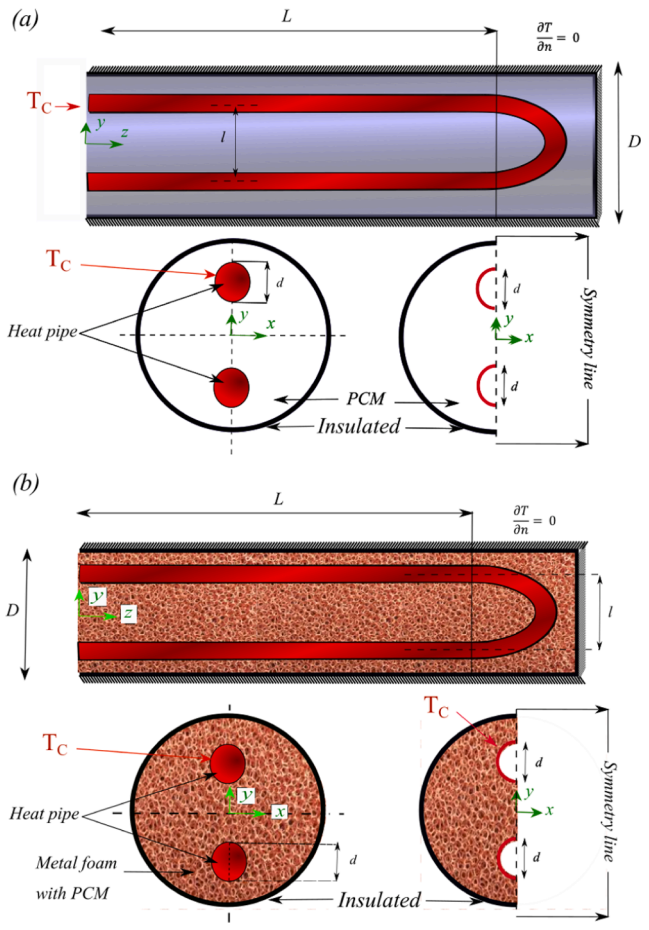

Fig. 1. A view of the heat exchanger geometry and physical model.

U-shape hot pipe. The space between the shell and the tube can be filled with paraffin or paraffin/copper metal foam. The external shell is adiabatic. The hot tube is at a constant hot temperature of T_h during the charging process or a cold temperature of T_c during the discharge process. The melting temperature of paraffin is T_f, in which $T_c < T_f < T_h$. The porous space is an open cell porous medium, and the natural convection flows are possible. In pure paraffin, the natural convection effects can be more significant and are taken into account.

A 2-D cross-section of the heat exchanger is selected as the computational domain. Moreover, due to the symmetry of the heat exchanger, the computations will be performed solely for half of the 2-D cross-section. It should be noted that in the case of non-horizontal placement of tubes, the symmetry of the model will be lost, and a full model with no symmetry should be used.

The governing equations for conservation of mass, flow, and heat in the heat exchanger can be written as:

$$\frac{\partial u}{\partial x}+\frac{\partial v}{\partial y}=0 \tag{1}$$

$$\frac{\rho_l}{\varepsilon}\frac{\partial u}{\partial t}+\frac{\rho_l}{\varepsilon^2}\left(u\frac{\partial u}{\partial x}+v\frac{\partial u}{\partial y}\right)=-\frac{\partial p}{\partial x}+\frac{\mu_l}{\varepsilon}\left(\frac{\partial^2 u}{\partial x^2}+\frac{\partial^2 u}{\partial y^2}\right)-\frac{\mu_l}{\kappa}u-s(T)u \tag{2}$$

$$\frac{\rho_l}{\varepsilon}\frac{\partial v}{\partial t}+\frac{\rho_l}{\varepsilon^2}\left(u\frac{\partial v}{\partial x}+v\frac{\partial v}{\partial y}\right)=-\frac{\partial p}{\partial y}+\frac{\mu_l}{\varepsilon}\left(\frac{\partial^2 v}{\partial x^2}+\frac{\partial^2 v}{\partial y^2}\right)+\rho_l g\beta_l(T-T_f)-\frac{\mu_l}{\kappa}v-s(T)v \tag{3}$$

$$(\rho C_p)_m\frac{\partial T}{\partial t}+(\rho C_p)_l\left(u\frac{\partial T}{\partial x}+v\frac{\partial T}{\partial y}\right)=k_m\left(\frac{\partial^2 T}{\partial x^2}+\frac{\partial^2 T}{\partial y^2}\right)-\varepsilon\rho_l h_{sf}\frac{\partial\phi(T)}{\partial t} \tag{4}$$

Table 1
The thermo-physical properties of the copper foam and paraffin wax [37,39].

Material	β (1/K)	ρ (kg/m^3)	c_p (J/kg·K)	k (W/m·K)	μ (Pa·s)	h_{sf} (J/kg·K)
Paraffin	0.0005	900	2300	0.3	0.00324	148,800
Copper foam	–	8900	386	380	–	–

The above equations are applicable for phase change with natural convection and fluid flow in a porous medium. Moreover, taking the porosity as unity and tending the permeability a large number removes the Darcy source term. The phase change equations reduce the phase change heat transfer of pure paraffin in a clear flow region with no porous matrix. Besides, the inertia terms are important in the liquid phase, and thus, the density of liquid PCM is considered as the reference density, and the density variations on the change phase were neglected. The l and m subscripts represent the liquid PCM and effective properties of PCM and porous medium (composite matrix), respectively. The effective thermal conductivity of the PCM and porous medium were computed [38,39] as 11.48 and 5.6 for the porosities of 0.9 and 0.95, respectively. The thermophysical properties of pure material are also reported in Table 1. The effective heat capacity was computed by employing the conservation of the energy as:

$$(\rho C_p)_m=\phi(\rho C_p)_{m,l}+(1-\phi)(\rho C_p)_{m,s} \tag{5a}$$

in which:

$$\begin{aligned}(\rho C_p)_{m,l}&=(1-\varepsilon)(\rho C_p)_p+\varepsilon(\rho C_p)_l,\\(\rho C_p)_{m,s}&=(1-\varepsilon)(\rho C_p)_p+\varepsilon(\rho C_p)_s\end{aligned} \tag{5b}$$

Assuming $\varepsilon \to 1$ and $\kappa \to \infty$, the model reduces to the case of pure paraffin. Moreover, assuming $g \to 0$, the model would represent the phase change heat transfer in the paraffin-graphene composite.

Following the introduced model, the initial and boundary conditions for the heat exchanger can be written as follows:

Initial and boundary conditions

In the case of the charging process, the heat exchanger is at a uniformly cold temperature of T_c, while in the case of the discharging process, the heat exchanger is at an even hot temperature of T_h. The shell wall adiabatic as $\frac{\partial T}{\partial n}=0$ where n indicates the normal surface vector.

The symmetry condition of the tube shell with diameter D at the symmetry line:

$$\frac{\partial T}{\partial x}=0,\quad \frac{\partial u}{\partial x}=0 \tag{6a}$$

The tube temperature in the charging process

$$T=T_c \quad \text{for } t<24s, \quad \text{and} \quad T=T_h \quad \text{for } t>24s \tag{6b}$$

The tube temperature in discharging process

$$T=T_h \quad \text{for } t<24s, \quad \text{and} \quad T=T_c \quad \text{for } t>24s \tag{6c}$$

The no-slip and fluid permeability boundary conditions are applied for the heat exchanger walls.

Source term

$$s(T)=A_{mush}\frac{(1-\phi(T))^2}{\phi(T)^3+e} \tag{7a}$$

$$\phi(T)=\begin{cases}0 & T<T_f\\ \dfrac{T-T_f}{\delta T} & T_f<T<T_f+\delta T\\ 1 & T>T_f+\delta T\end{cases} \tag{7b}$$

The symbols of ε and κ stand for the metal foam porosity and its permeability. Here, ϕ denotes the molten volume fraction.

In order to generalize the solution, the governing Eqs. (1)–(7) were transformed into a dimensionless format invoking the following scale variables:

$$X=\frac{x}{H}, Y=\frac{y}{H}, U=\frac{uH}{\alpha_l}, V=\frac{vH}{\alpha_l}, \theta=\frac{T-T_\infty}{\Delta T}, \tau=\frac{t\alpha_l}{H^2}, S(\theta)=\frac{s(T)H^2}{\rho_l\alpha_l}$$
$$P=\frac{pH^2}{\rho\alpha_l^2}, \alpha_l=\frac{k_l}{(\rho c_p)_l}, Pr=\frac{\nu}{\alpha_l}, Ra=\frac{g\beta_l\Delta TH^3}{\nu_l\alpha_l}, Ste=\frac{Cp_l\Delta T}{h_{sf}}, Da=\frac{\kappa}{H} \quad (8)$$

where $H = D$ shows the characteristic length, Pr and Ra indicate the Prandtl and the Rayleigh numbers. The temperature scale (ΔT) was adopted as $\Delta T = T_h$-T_c. Rayleigh number of a porous medium could be commonly introduced as the product of the traditional Rayleigh (in pure fluid) number and Darcy number ($Ra_{porous} = Ra \times Da$) and is known as the Darcy-Rayleigh number. It should be noted that the product of the Rayleigh number and Darcy number could represent the strength of natural convection in a porous medium. The Darcy-Rayleigh number is of interest in Darcy models since there is no Darcy number involved. In the present study, the Darcy-Brinkman approach was used, and hence, the Rayleigh number in its typical form was derived. Since both Darcy and Rayleigh numbers are available, the Darcy-Rayleigh number is simply equal to $Da \times Ra$.

The geometrical non-dimensional parameter is $E_c = l/H$. Eventually, the dimensionless governing equations were achieved by plugging Eq. (8) into Eqs. (1)–(7) as:

x and y momentum equations:

$$\frac{1}{\varepsilon}\frac{\partial U}{\partial \tau}+\frac{1}{\varepsilon^2}\left(U\frac{\partial U}{\partial X}+V\frac{\partial U}{\partial Y}\right)=-\frac{\partial P}{\partial X}+A(\phi)\frac{Pr}{\varepsilon}\left(\frac{\partial^2 U}{\partial X^2}+\frac{\partial^2 U}{\partial Y^2}\right)-\frac{Pr}{Da}U-S(\theta)U \quad (9)$$

$$\frac{1}{\varepsilon}\frac{\partial V}{\partial \tau}+\frac{1}{\varepsilon^2}\left(U\frac{\partial V}{\partial X}+V\frac{\partial V}{\partial Y}\right)=-\frac{\partial P}{\partial Y}+A(\phi)\frac{Pr}{\varepsilon}\left(\frac{\partial^2 V}{\partial X^2}+\frac{\partial^2 V}{\partial Y^2}\right)+PrRa\theta-\frac{Pr}{Da}V-S(\theta)V \quad (10)$$

Energy in metal foam-PCM:

$$\left(\phi\frac{(\rho C_p)_{m,l}}{(\rho C_p)_l}+(1-\phi)\frac{(\rho C_p)_{m,s}}{(\rho C_p)_l}\right)\frac{\partial\theta}{\partial\tau}+\left(U\frac{\partial\theta}{\partial X}+V\frac{\partial\theta}{\partial Y}\right)=\frac{k_m}{k_l}\left(\frac{\partial^2\theta}{\partial X^2}+\frac{\partial^2\theta}{\partial Y^2}\right)-\frac{\varepsilon}{Ste}\frac{\partial\phi(\theta)}{\partial\tau} \quad (11)$$

Ste represents the Stefan number, and A(ϕ) artificially controls the PCM's viscosity in the solid region and aids the convergence. Here, $A(\phi) = 1+(1\text{-}\phi)/(\rho\alpha)_l$, and it artificially promotes the viscosity ratio in the solid domain.

The non-dimensional initial temperatures are $\theta = 0$ for charging and $\theta = 1$ for discharging cases. The non-dimensional outer wall is adiabatic as:

$$\frac{\partial\theta}{\partial N}=0 \quad (12a)$$

where $N = n/H$ is the non-dimensional normal vector of the surface.

The non-dimensional symmetry condition leads to:

$$\frac{\partial\theta}{\partial X}=0,\ \frac{\partial U}{\partial X}=0, \text{ at symmetry line} \quad (12b)$$

The non-dimensional tube temperature in charging process

$$\theta=0 \text{ for } \tau<0.0124 \text{ and } \theta=1 \text{ for } \tau>0.0124 \quad (12c)$$

The tube temperature in discharging process

$$\theta=1 \text{ for } \tau<0.0124 \text{ and } \theta=0 \text{ for } \tau>0.0124 \quad (12d)$$

The thermophysical ratios are summarized as:

$$\frac{k_{m,s}}{k_l}\sim\frac{k_{m,l}}{k_l}\sim\frac{k_m}{k_{m,l}},\ \frac{(\rho C_p)_{m,s}}{(\rho C_p)_l}=(1-\varepsilon)\frac{(\rho C_p)_p}{(\rho C_p)_l}+\varepsilon\frac{(\rho C_p)_s}{(\rho C_p)_l},\ \frac{(\rho C_p)_{m,l}}{(\rho C_p)_l}=(1-\varepsilon)\frac{(\rho C_p)_p}{(\rho C_p)_l}+\varepsilon,\ \frac{(\rho C_p)_s}{(\rho C_p)_l}\sim 1 \quad (13)$$

$$\phi(\theta)=\begin{cases}0 & \theta\leqslant\theta_f-\frac{1}{2}\delta\theta\\ \frac{\theta-\theta_f}{\delta\theta}+\frac{1}{2} & \theta_f-\frac{1}{2}\delta\theta<\theta<\theta_f+\frac{1}{2}\delta\theta\\ 1 & \theta\geqslant\theta_f+\frac{1}{2}\delta\theta\end{cases} \quad (14)$$

where $\theta_f = (T_f\text{-}T_\infty)/\Delta T$.

The Nusselt number is defined as $Nu = h \times H/k_l$. Here, h shows the convective heat transfer coefficient, and it was obtained by the surface energy balance as $k_m(\partial T/\partial n) = h\times(T_h\text{-}T_c)$, which leads to $h = k_m(\partial T/\partial n)/\Delta T$. Consequently, $Nu = (k_m/k_l)(\partial\theta/\partial N)$. Using the relations for thermal conductivity ratios and assuming $k_{m,l} = k_{m,s}$, Nusselt number can be written as below:

$$Nu_{l,top}=-\left[(1-\varepsilon)\frac{k_s}{k_f}+\varepsilon(1+Nc\phi)\right]\left(\frac{\partial\theta}{\partial n}\right)_{C_{top}} \quad (15a)$$

$$Nu_{l,bottom}=-\left[(1-\varepsilon)\frac{k_s}{k_f}+\varepsilon(1+Nc\phi)\right]\left(\frac{\partial\theta}{\partial n}\right)_{C_{bottom}} \quad (15b)$$

where the subscripts of top and bottom denote the top and hot bottom tubes, respectively.

The integration of the above equations leads to the total heat transfer rate:

$$Nu_{a,top}=\frac{1}{\pi}\int_0^\pi Nu_{l,top}d\omega \quad (16a)$$

$$Nu_{a,bottom}=\frac{1}{\pi}\int_0^\pi Nu_{l,bottom}d\omega \quad (16b)$$

$$Nu_{a,total}=\frac{Nu_{a,top}+Nu_{a,bottom}}{2} \quad (16c)$$

where ω is the differential element for the arc of the hot wall, and the subscript of total shows the average Nusselt number for both hot tubes.

Eventually, the total molten fraction was computed as:

$$MVF=\frac{\int_A\varepsilon\phi dA}{\int_A\varepsilon dA} \quad (17)$$

The permeability of the metal foam was computed following model of Tian and Zhao [40].

The size of the heat storage unit is $H = D = 100$ mm, and the heated tube diameter is $d = 17$ mm. The other geometrical details can be easily deduced from the non-dimensional parameters. The following primary initial/boundary conditions were adopted for the simulations: $T_c = 308$ K, $T_h = 338$ K, and $T_f = 323$ K.

3. Numerical method, mesh study, and validation

3.1. The numerical method

The governing equations were integrated by employing the finite element method (FEM). The weak form of FEM equations was integrated numerically on the mesh domain.

The phase change phenomena take place in a limited range of temperatures. There is an intense temperature gradient at the phase change interface (melting front) because of the natural convection. This significant gradient at the melting front zone caused the temperature to

change in a narrow region rapidly. Consequently, the phase change would take place in a slender ribbon around the phase-change interface. Thus, achieving accurate results requires miniature mesh elements. Thus, capturing the phase change with a static mesh demands a huge number of elements and could also lead to the numerical instability.

Furthermore, there is a strong velocity gradient at the melting front as the free convection velocities of the molten region are transient to zero in the solid domain. Thus, not only the temperature gradients are high at the melting region, but also the hydrodynamic gradients are also notable in the slender mushy region. The thermophysical changes and variation of the latent heat of melting would also take place in this region. So, these phenomena lead to extreme non-linear and unstable equations in the phase change problems. As a solution to such problems, an adaptive mesh technique was used to locally improves the mesh resolution in the mushy region. The mesh-adaptation tracks the phase change region dynamically and improves the accuracy of the solution.

An automatic time-step scheme based on the backward differentiation formula (BDF) was implemented to control the time-step selection and maintain the accuracy of the computations and reduce the computational times. Following the FEM, a basis set $\{\gamma_k\}_{k=1}^{N}$ was introduced, so the x-velocity, y-velocity, pressure, and temperature are developed as follows:

$$\begin{aligned} U &\approx \sum_{m=1}^{N} U_m \gamma_m(X,\ Y),\\ V &\approx \sum_{m=1}^{N} V_m \gamma_m(X,\ Y),\\ P &\approx \sum_{m=1}^{N} P_m \gamma_m(X,\ Y),\\ \theta &\approx \sum_{m=1}^{N} \theta_m \gamma_m(X,\ Y) \end{aligned} \tag{18}$$

The linear function was applied for the temperature and pressure. The provided grid elements were triangles. Also, the basis function utilized for the variable γ was the same as the other parameters. Thus, by employing the Galerkin FEM and integrating the governing equation over the domain of solution, the residual equations were obtained as follows:

$$\begin{aligned} R_i^1 \approx{}& \frac{1}{\varepsilon}\sum_{m=1}^{N} U_m \int \frac{\partial \gamma_m}{\partial \tau}\gamma_i dXdY + \frac{1}{\varepsilon^2}\sum_{m=1}^{N} U_m \int\left[\left(\sum_{m=1}^{N} U_m\gamma_m\right)\frac{\partial \gamma_m}{\partial X} + \left(\sum_{k=1}^{N} V_m\gamma_m\right)\frac{\partial \gamma_m}{\partial Y}\right]\gamma_i dXdY\\ &+\sum_{m=1}^{N}\int\left(-\sum_{m=1}^{N} P_m\gamma_m\right)\frac{\partial \gamma_m}{\partial X}\gamma_i dXdY + A(\phi)\frac{2Pr}{\varepsilon}\sum_{m=1}^{N} U_m\int\frac{\partial \gamma_m}{\partial X}\frac{\partial \gamma_i}{\partial X}dXdY\\ &+A(\phi)\frac{Pr}{\varepsilon}\sum_{m=1}^{N} U_m\int\left[\frac{\partial \gamma_m}{\partial Y}\frac{\partial \gamma_i}{\partial Y}\right]dXdY + A(\phi)\frac{Pr}{\varepsilon}\sum_{m=1}^{N} V_m\int\frac{\partial \gamma_m}{\partial X}\frac{\partial \gamma_i}{\partial Y}dXdY\\ &-A(\phi)\frac{Pr}{Da}\int\left(\sum_{m=1}^{N} U_m\gamma_m\right)\gamma_i dXdY - S(\theta)\int\left(\sum_{m=1}^{N} U_m\gamma_m\right)\gamma_i dXdY \end{aligned} \tag{19a}$$

$$\begin{aligned} R_i^2 \approx{}& \frac{1}{\varepsilon}\sum_{m=1}^{N} V_m \int \frac{\partial \gamma_m}{\partial \tau}\gamma_i dXdY + \frac{1}{\varepsilon^2}\sum_{m=1}^{N} V_m \int\left[\left(\sum_{m=1}^{N} U_m\gamma_m\right)\frac{\partial \gamma_m}{\partial X} + \left(\sum_{k=1}^{N} V_m\gamma_m\right)\frac{\partial \gamma_m}{\partial Y}\right]\gamma_i dXdY\\ &+\sum_{m=1}^{N}\int\left(-\sum_{m=1}^{N} P_m\gamma_m\right)\frac{\partial \gamma_i}{\partial Y}dXdY + A(\phi)\frac{2Pr}{\varepsilon}\sum_{m=1}^{N} V_m\int\frac{\partial \gamma_m}{\partial Y}\frac{\partial \gamma_i}{\partial Y}dXdY\\ &+A(\phi)\frac{Pr}{\varepsilon}\sum_{m=1}^{N} U_m\int\left[\frac{\partial \gamma_m}{\partial Y}\frac{\partial \gamma_i}{\partial X}\right]dXdY + A(\phi)\frac{Pr}{\varepsilon}\sum_{m=1}^{N} V_m\int\frac{\partial \gamma_m}{\partial X}\frac{\partial \gamma_i}{\partial X}dXdY\\ &-A(\phi)\frac{Pr}{Da}\int\left(\sum_{m=1}^{N} V_m\gamma_m\right)\gamma_i dXdY - S(\theta)\int\left(\sum_{m=1}^{N} V_m\gamma_m\right)\gamma_i dXdY + PrRa\int\left(\sum_{m=1}^{N}\theta_m\gamma_m\right)\gamma_i dXdY \end{aligned} \tag{19b}$$

$$R_i^3 \approx \sum_{m=1}^{N} U_m\int\frac{\partial \gamma_m}{\partial X}\gamma_i dXdY + \sum_{m=1}^{N} V_m\int\frac{\partial \gamma_m}{\partial Y}\gamma_i dXdY \tag{19c}$$

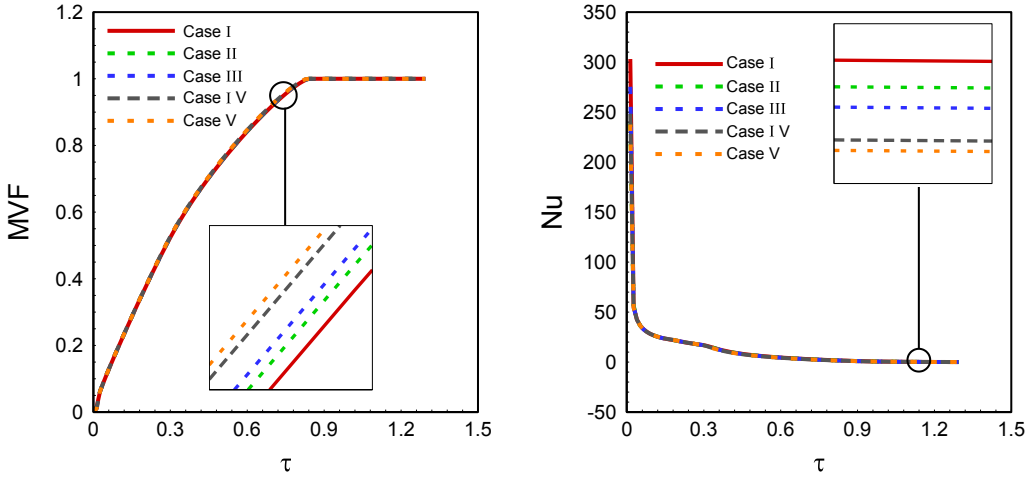

Fig. 2. The dependency of the *MVF and Nu* number of upside heat pipe as a function of τ on the grid size for metal-foam structure.

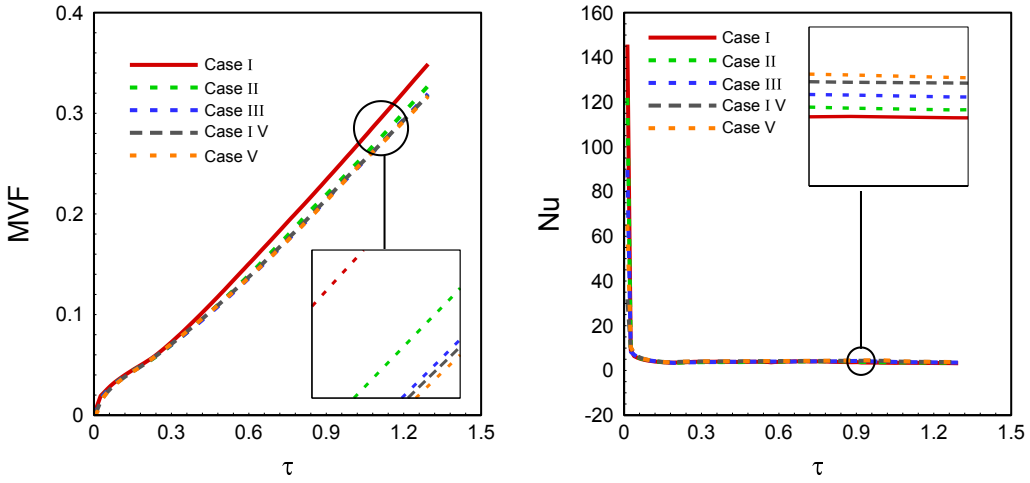

Fig. 3. The dependency of the *MVF and Nu* number of upside heat pipe as a function of τ on the grid size for pure paraffin structure.

$$R_i^4 \approx \left(\phi + (1-\phi)\frac{(\rho C_p)_{m,s}}{(\rho C_p)_{m,l}}\right)\sum_{m=1}^{N}\theta_m \int \frac{\partial \gamma_m}{\partial \tau}\gamma_i dXdY + \left(\frac{(\rho C_p)_{m,l}}{(\rho C_p)_l}\right)^{-1}\sum_{m=1}^{N}\theta_m \int\left[\left(\sum_{m=1}^{N}U_m\gamma_m\right)\frac{\partial \gamma_m}{\partial X}+\left(\sum_{m=1}^{N}V_m\gamma_m\right)\frac{\partial \gamma_m}{\partial Y}\right]\gamma_m dXdY + \frac{k_m}{k_{m,l}}\sum_{m=1}^{N}\theta_k\int\left[\frac{\partial \gamma_m}{\partial X}\frac{\partial \gamma_i}{\partial X}+\frac{\partial \gamma_m}{\partial Y}\frac{\partial \gamma_i}{\partial Y}\right]dXdY - \frac{1}{Ste}\sum_{m=1}^{N}\frac{\partial \phi(\theta_m)}{\partial \theta}\int\frac{\partial \gamma_m}{\partial \tau}\gamma_i dXdY \tag{19d}$$

where

$$\frac{\partial \phi(\theta)}{\partial \theta} = \begin{cases} 0 & \theta \leqslant \theta_f - \frac{1}{2}\delta\theta \\ \frac{1}{\delta\theta} & \theta_f - \frac{1}{2}\delta\theta < \theta < \theta_f + \frac{1}{2}\delta\theta \\ 0 & \theta \geqslant \theta_f + \frac{1}{2}\delta\theta \end{cases} \tag{20}$$

The residual equations were integrated by Gaussian quadrature with second-order accuracy. For the grid adaptation, the melt volume fraction ϕ_{adapt} was used with a wider temperature range near the phase change region and a broader domain. The following function (adaptation area) is expanded as follows:

$$\phi_{adapt}(\theta) = \begin{cases} 0 & \theta \leqslant \theta_f - \frac{3}{2}\delta\theta \\ 1 & \theta_f - \frac{3}{2}\delta\theta < \theta < \theta_f + \frac{3}{2}\delta\theta \\ 0 & \theta \geqslant \theta_f + \frac{3}{2}\delta\theta \end{cases} \tag{21}$$

where the adaptation occurs at the space signed with $\phi_{adapt} = 1$. The adaptation area takes place around the melting front. The adaptation region is a little wider than the actual mushy region and allows a continuous mesh transition from local miniature size to usual mesh sizes in the enclosure. Moreover, the wider mesh adaptation region ensures that the mushy region remains inside the adapted area. As a result, the mesh adaptation could be skipped for some intermediate time-steps, which eventually reduces the overall computational time. As long as the volume fraction $\phi_{adapt} = 1$, and the considered area covers the melting front, there is no need for a new grid adaptation. Whenever the mushy region reaches the boundaries of the adopted region $\phi_{adapt} = 1$), the new grid adaption should be done. The elements of the adapted region were five fold finer (smaller) than the typical meshes in the enclosure.

The mesh adaptation was used to track the melting interface during the phase change and provide high-resolution mesh at the phase change region. Since the mesh adaptation is a computationally costly, it was

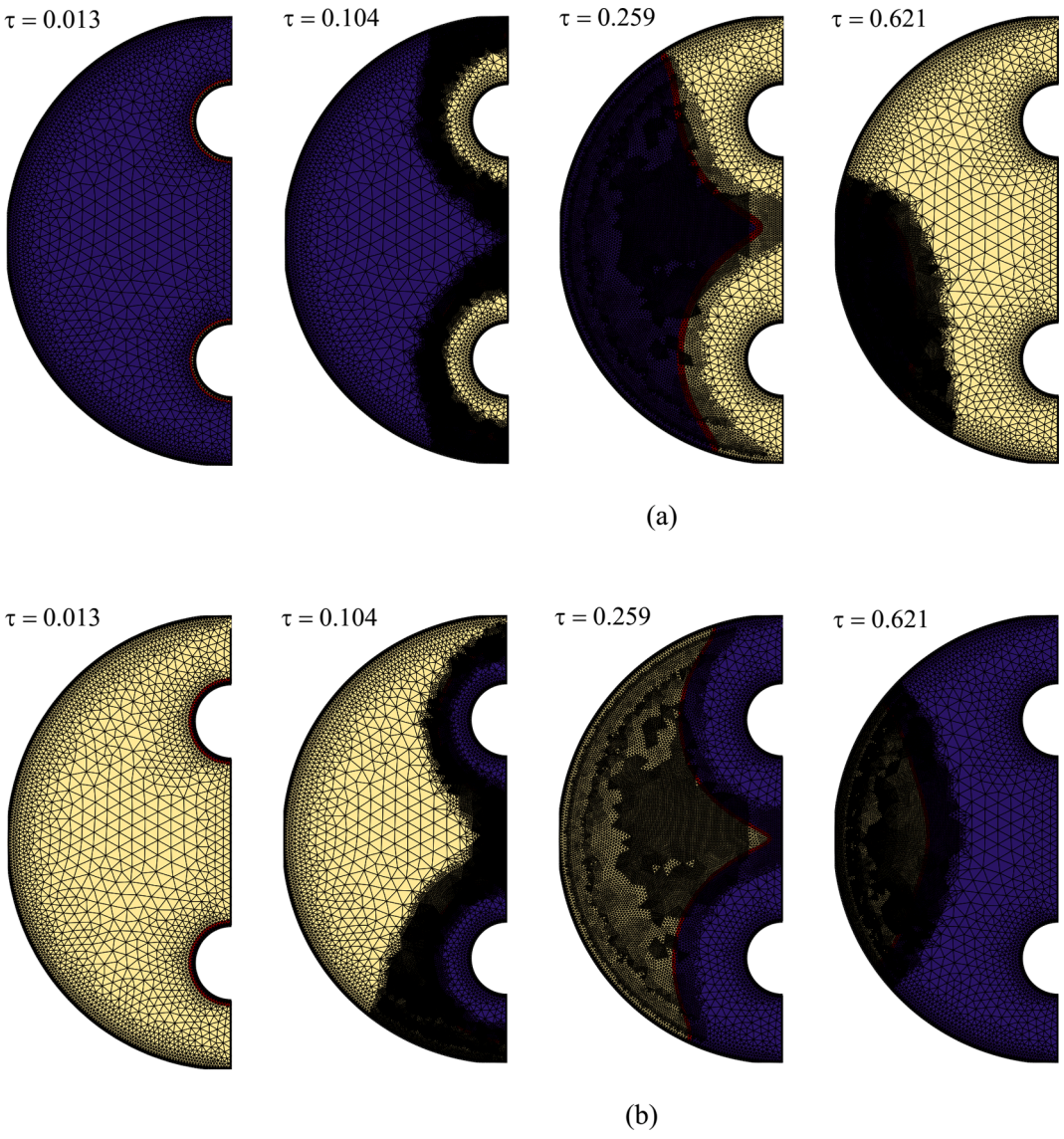

Fig. 4. The mesh adaptation for Case III for (a): melting process and (b): solidification process.

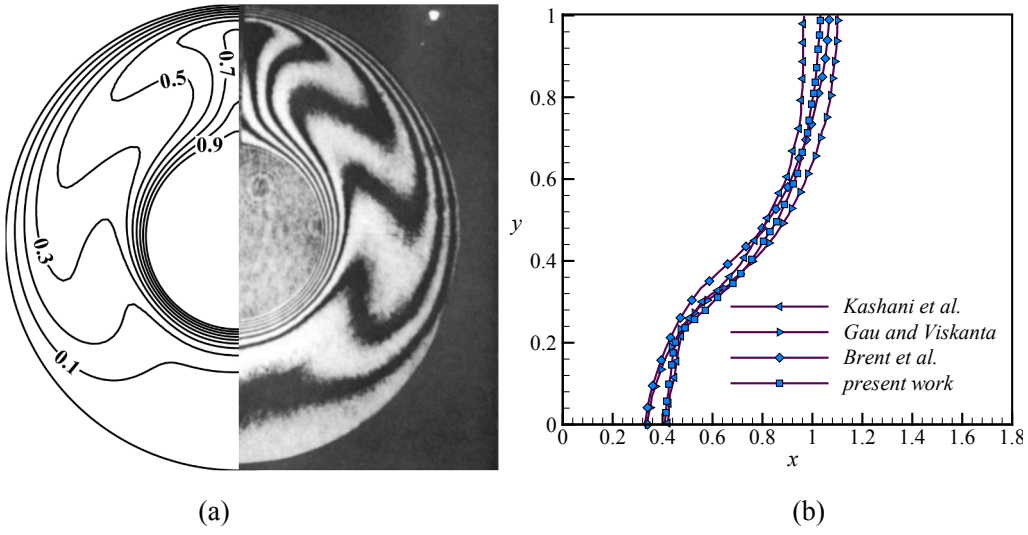

Fig. 5. (a) Comparison between temperature of the present study (left) and experimental one (right) [45] for $Pr = 0.706$ and $Ra = 4.7 \times 10^4$. (b) Comparison of melting interface with the benchmark investigations of [47–49] and current phase change simulations.

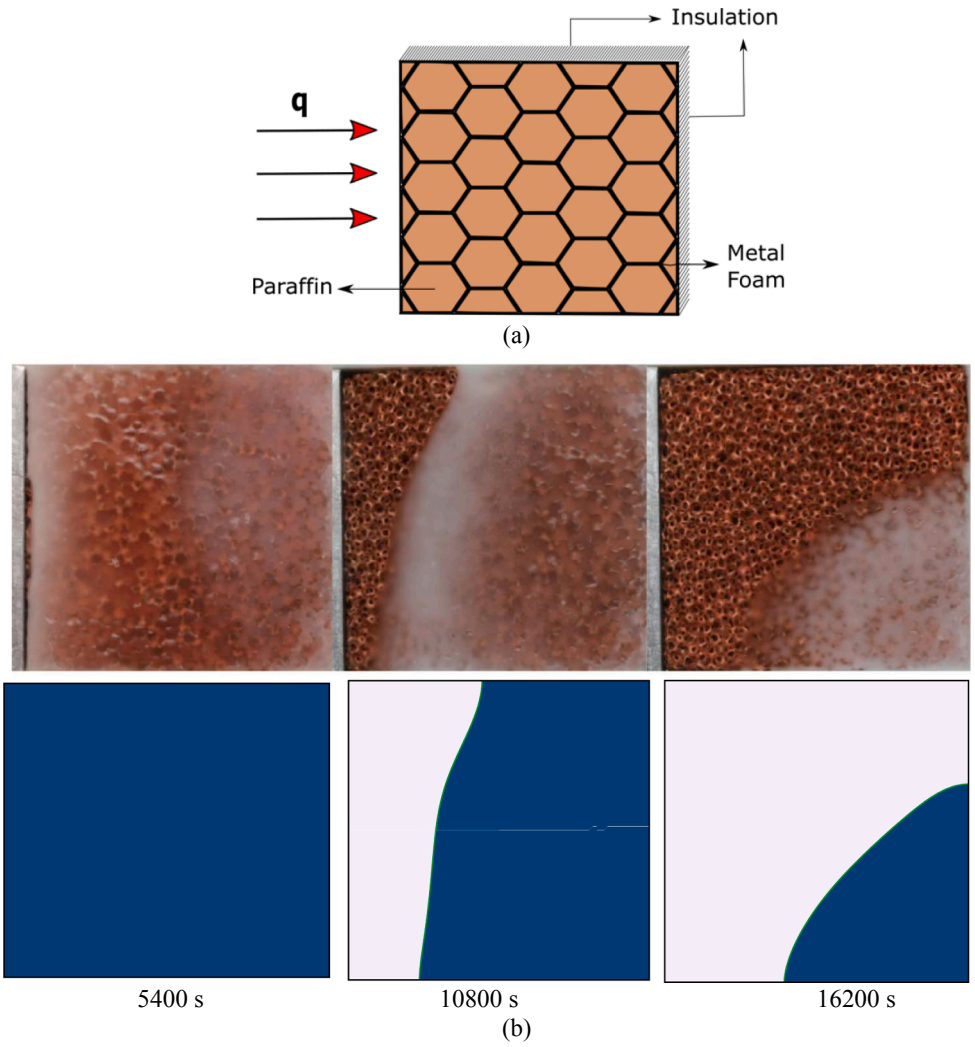

Fig. 6. Comparison of the results with the study of Zheng et al. [39]; (a) Physical model and (b) Melting interface in the experimental study (first row) and the present computations (second row).

checked and performed every 25 s ($\tau = 0.0129$). The heating time was started at 25 s ($\tau = 0.0129$), which is just one second before the first adaptation. Thus, just one second after the commencing of phase change heat transfer, the first mesh adaptation check would be applied at $t = 25$ s ($\tau = 0.0129$) and ensures the high resolution of mesh at the phase change region. The hot tubes' heating time could be any arbitrary time, but setting it as 24 s ($\tau = 0.0124$) is convenient for the mesh adaptation computations as adopted in Eq. (6).

As mentioned, a BDF automatic time step was used to adjust the computational time-steps [41]. The Newton method with A PARDISO solver [42–44] was utilized to solve the residual equations iteratively, and the order of residual error was 10^{-6}. The damping factor was

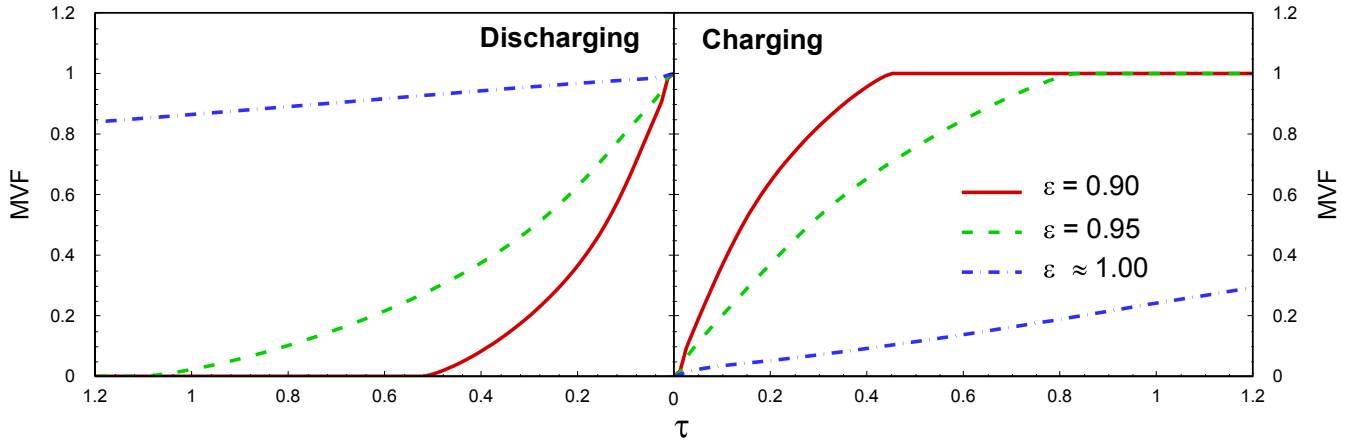

Fig. 7. The value of melting volume fraction (*MVF*) against dimensionless time.

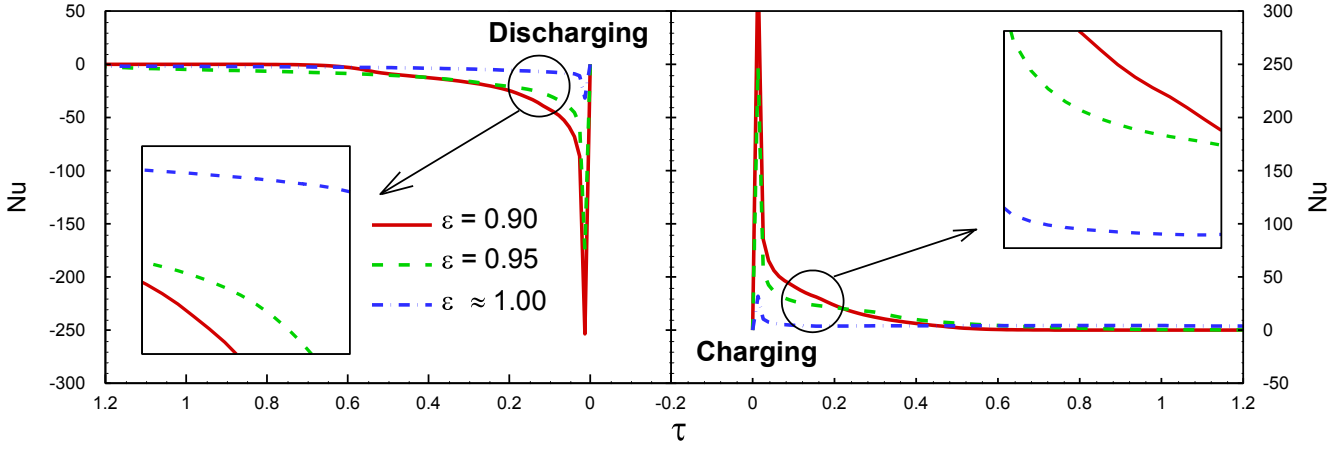

Fig. 8. The value of *Nu* from upside heat pipe against dimensionless time.

considered 0.9. By estimating some dimensionless parameters, the mesh study and validation were conducted.

3.2. Mesh study

The grid study is very important to achieve accurate results in all numerical studies. Five different grids with different element numbers (case I = 1100, case II = 1415, case III = 1927, case IV = 4768 and case V = 11626) were examined for this study. The mesh is dense at the walls to better capture the wall effects. The melt volume fraction (MVF) and Nusselt number on the upside heat pipe were examined at different time-steps for different element numbers. Fig. 2 shows the time history of MVF and Nu for the metal foam structure, and Fig. 3 demonstrates them for the pure paraffine structure. It can be seen that there is an inconsiderable difference between the results of case III, case IV, and case V. Thus, due to the decrease in the cost and time of numerical simulations, case III was chosen for all studies.

Furthermore, the initial mesh and its deformation versus the time for melting and solidification processes are shown in Fig. 4(a), (b). According to these figures, a smooth transient grid size is apparent. Fig. 4 (a) shows the phase change heat transfer at the beginning of the charging process, where the enclosure is filled with solid PCM. At the beginning of heat transfer ($\tau = 0.13$), the mesh is typical with no adaptation. During the time, the phase change commences from the hot tubes ($\tau = 0.104$) and advances toward the sell. The melting interface is with a small distance from the tubes, and as seen, the mesh dense around the melting interface.

It should be noted that now the mesh at the vicinity of tubes is regular as the melting interface has already passed this region. After this stage, the melting interface advances toward the shell, and dense mesh covers a large region of the shell since this area is under the potential influence of the phase change interface. At the final stage of melting ($\tau = 0.621$), the mesh has only concentrated at the remaining solid region where the phase change is taking place.

Figure 4(b) shows the discharging process where the enclosure is fully melted, and the solidification starts. In the beginning, the mesh is typical, with no adaptation($\tau = 0.13$). Then, solidification takes place around the tubes and advances toward the shell. A dense mesh follows the phase change regions as the solidification interface moves away from tubes. When the solidification interface passes a region, the mesh returns to its typical coarse size. It should be noted that the utilized fixed mesh with no adaptation cannot capture a high-resolution narrow phase change bond and is not capable of solving the model.

3.3. Verification and validation

Kuehn and Goldstein [45] examined the natural convection heat transfer in the space between two horizontal cylinders. Their experimental outcomes are compared with the isotherms of the present study when $Pr = 0.706$ and $Ra = 4.7 \times 10^4$. As seen in Fig. 5, both studies are a good match.

The melting interface was computed with the same conditions as stated in the benchmark study of Bertrand et al. [46], and the computed interface has been plotted in Fig. 5(b). The melting commences from the left hot wall and advances to the right. All surfaces are adiabatic except the right wall, which is heated. The melting interface has been plotted at

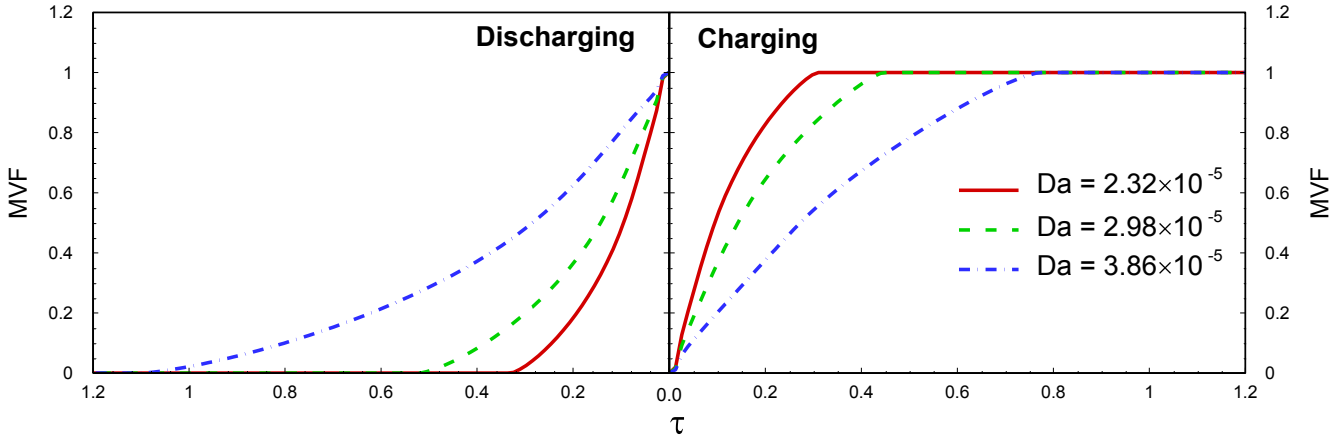

Fig. 9. The alteration of MVF over dimensionless time in different Da.

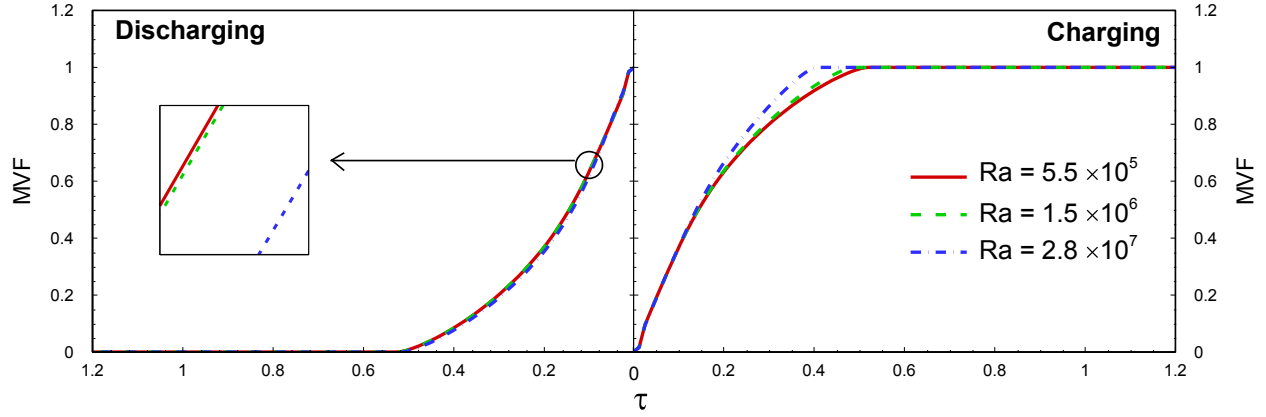

(a): $\varepsilon = 0.90$

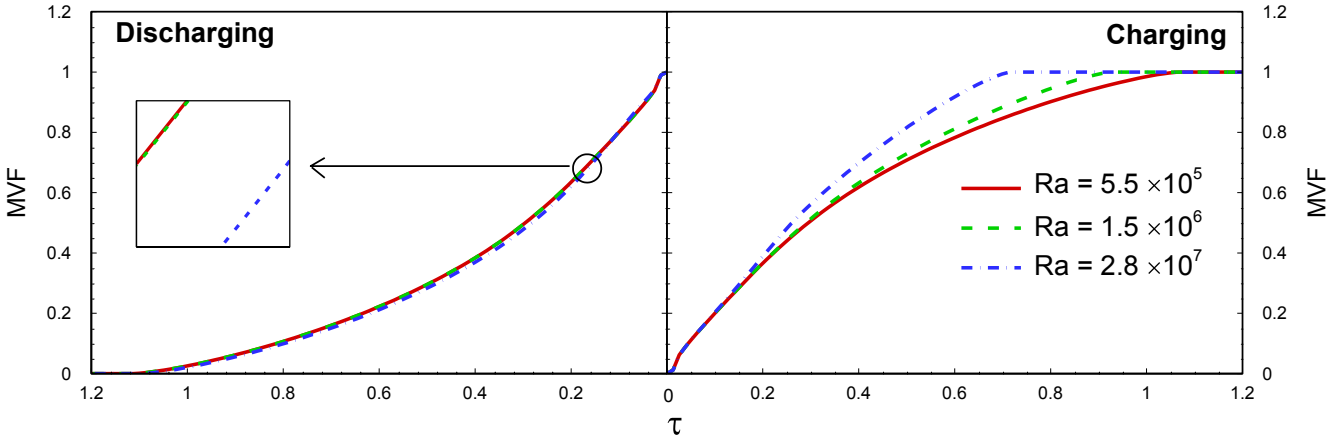

(b): $\varepsilon = 0.95$

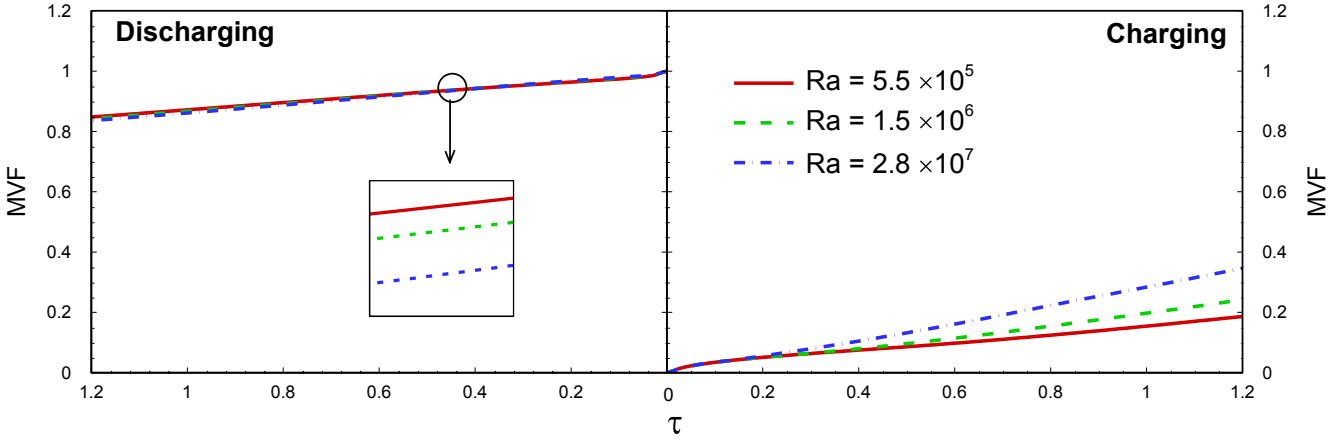

(c): $\varepsilon \approx 1$

Fig. 10. The effect of Ra number on melting volume fraction *(MVF)* over dimensionless time.

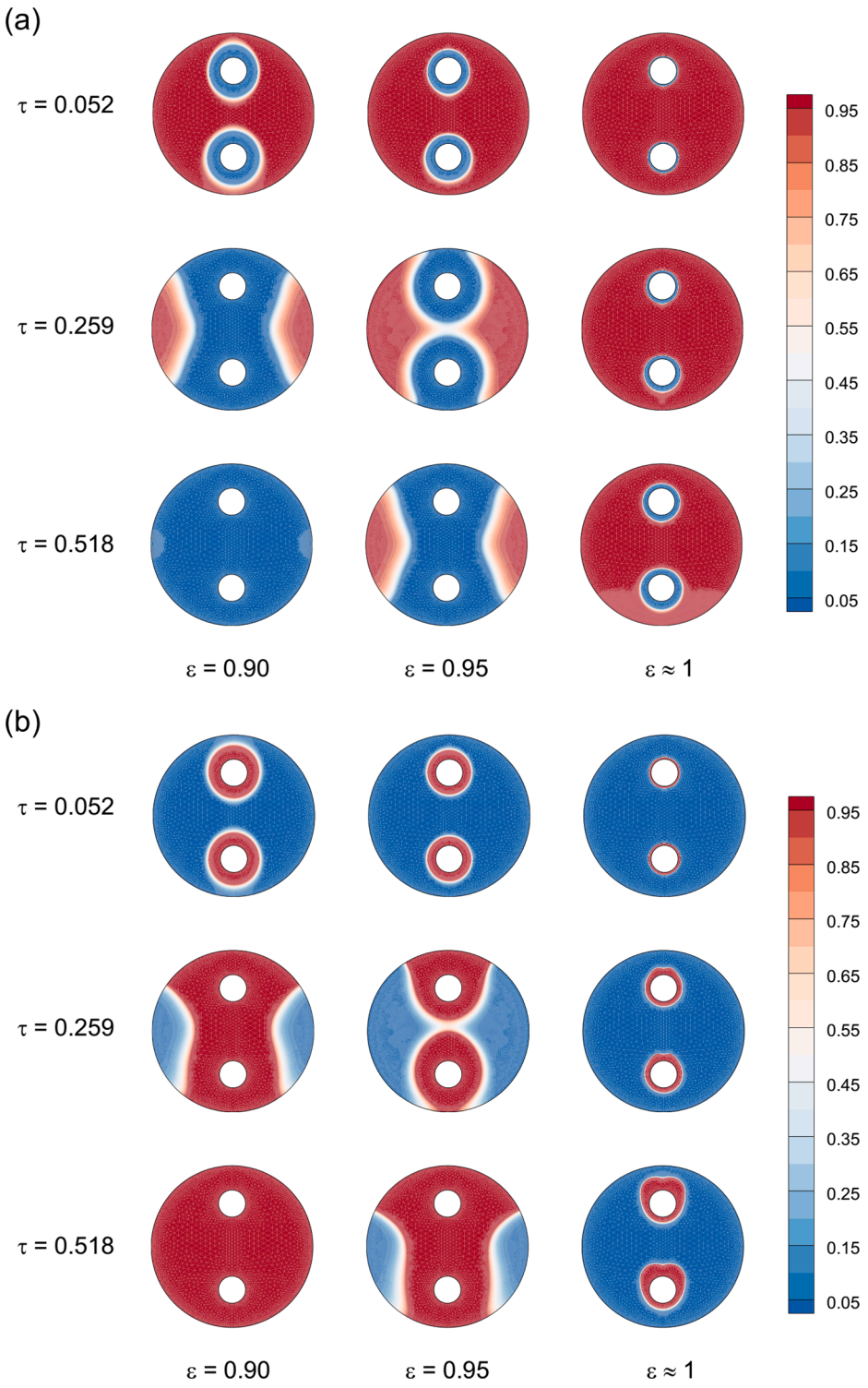

Fig. 11. The effect of Ra number on melting volume fraction *(MVF)* over dimensionless time (a): Discharging, (b): Charging.

two time-steps of $\tau = 2.05$ and $\tau = 3.48$ when *Ra* and *Pr* numbers are 1.25×10^5 and 50, respectively. Fig. 5(b) shows a good agreement between the captured melting interface and literature works.

In the case of melting heat transfer in a metal foam porous medium, the outcomes of the present study are compared with the experimental outcomes of Zheng et al. [39] for phase change of paraffin wax embedded in a metal foam. The cavity size was 0.1 m cavity occupied with a 5 PPI copper foam of $\varepsilon = 0.95$. The cavity walls were isolated except the left was, which was exposed to a constant heat flux of $q = 1150$ W/m^2 with a total heat loss of 7.5%. The melting interfaces are compared in Fig. 6, which shows good agreement.

4. Results and discussion

The simulations were performed for a typical case with the following dimensionless parameters: $\theta_f = 0.5$, $\varepsilon = 0.95$, $Pr = 1.2965$, $Ra = 1.4721 \times 10^7$, and $Da = 2.7 \times 10^{-5}$. The results will be reported for this set of the non-dimensional parameters, and if any variables changes, it will be

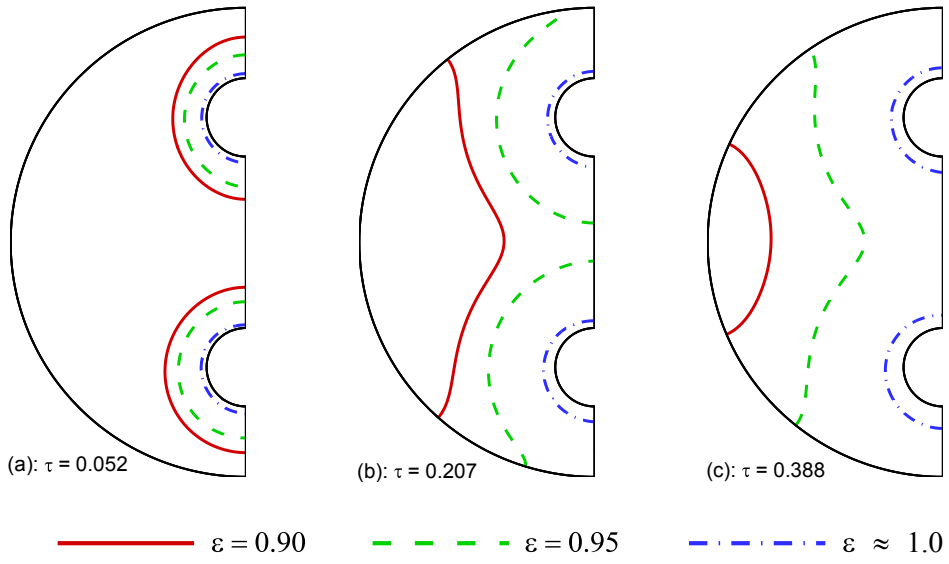

Fig. 12. Displacement of the boundary between solid and liquid interface at $MVF = 0.5$ during discharging mode: - $\varepsilon = 0.9$, - $\varepsilon = 0.95$, and - $\varepsilon \approx 1$.

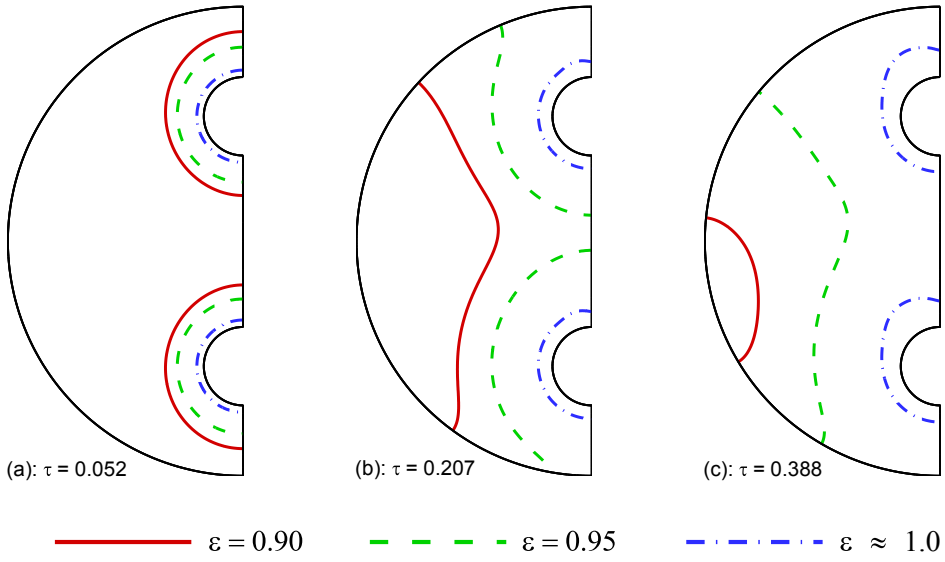

Fig. 13. Displacement of the boundary between solid and liquid interface at $MVF = 0.5$ during charging mode: - $\varepsilon = 0.9$, - $\varepsilon = 0.95$ and - $\varepsilon \approx 1$.

stated in the text.

Figure 7 shows the variation of the value of the melting volume fraction (MVF) as a function of time during charging and discharging for different values of ε. In charging mode, the MVF increases abruptly with time for $\varepsilon = 0.9$ and $\varepsilon = 0.95$ until reaching the value of 1, i.e., when the whole PCM in the cavity has melted. The fastest rate of melting is obtained for $\varepsilon = 0.9$. The increase of MVF substantially slower for $\varepsilon = 1$, and full melting is not reached for the time range of the plot. A similar behavior, but in the opposite direction, is observed during discharging. As the pipe is cooling down, the MVF decreases and reaches the value of 0 for $\varepsilon = 0.9$ and $\varepsilon = 0.95$. The quickest solidification is achieved for $\varepsilon = 0.9$. The solidification is much slower for $\varepsilon = 1$, and full solidification of the PCM is not achieved. Indeed, reducing ε increases the size of the solid matrix, which enhances the thermal conductivity of the PCM and contributes to a faster phase change during solidification or melting.

The variation of Nusselt number Nu for various values of ε as a function of time during charging and discharging is plotted in Fig. 8. Nu reaches a high value during charging, then starts to decrease significantly in all the cases before slowly reaching the steady value of zero, indicating that heat transfer has stopped. The high value of the Nusselt number at the beginning of each phase change problem is due to PCM's low thermal conductivity. At the beginning of the solidification process, the tubes' surface is directly exposed to molten PCM. When the first layer of solid PCM forms over the tube, this layer acts as thermal insulation over the tube and reduces the heat transfer rate (Nusselt number). In the case of melting heat transfer, the layer of solid PCM is directly in contact with the tube's surface. As melting advances, a layer of liquid PCM forms between the melting interface and the tube's surface, which limits the heat transfer rate. Thus, just after the phase change, the Nusselt number value drastically drops.

During the decrease, Nu is higher for lower ε and is maximum for $\varepsilon = 0.9$. Similarly, during the discharge, an abrupt increase of Nu is obtained before a slow stabilization toward zero value. In this case, Nu is negative, indicating that heat transfer is in the opposite direction. The absolute

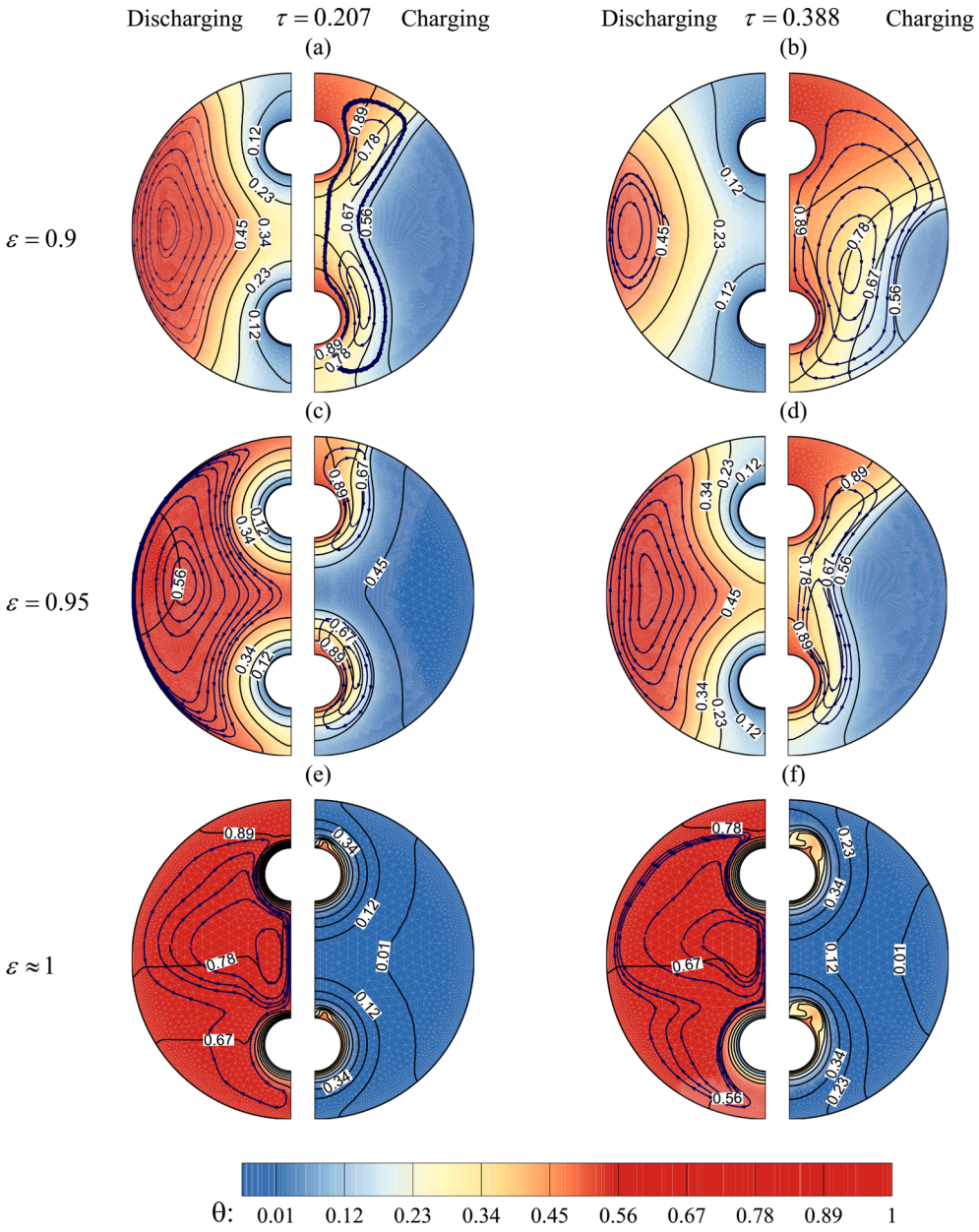

Fig. 14. Isotherm and contours for different porosity at various times.

value of *Nu* is also higher when ε is decreased and is at its highest value for $\varepsilon = 0.9$, indicating a better heat transfer when the porosity is decreased. This is due to the fact that the temperature is transmitted faster in the PCM because of the increased thermal conductivity resulting from the reduction of the foam porosity.

Figure 9 represents the effect of Darcy number on the phase change process in both charging and discharging modes. It can be observed that the span of the charging and discharging processes increase when the Darcy number changes from 2.32×10^{-5}to3.86×10^{-5}. Darcy number represents the effect of permeability of the porous medium, in which the higher value of Da indicates the better permeability. Therefore, the fluid can flow with higher velocity in the porous medium. Increasing the velocity, increasing convection heat transfer decreases the contact time between PCM and metal foam with a high conduction heat transfer coefficient. Therefore, the charging and discharging processes are boosted in lower Da due to greater contact time between PCM and metal foam.

Figure 10 depicts the variation of MVF as a function of time during charging and discharging for various values of the Rayleigh number, *Ra*, and the porosity, ε. During charging, it is shown that for all the values of ε, a higher increase of the MVF occurs when *Ra* is increased, and the full melting is achieved faster for higher values of *Ra*. On the other hand, the effect of *Ra* is less apparent in discharging mode, where a slightly faster solidification rate is observed when *Ra* is increased. In fact, *Ra* is an indicator of the relative importance of the buoyancy forces. As the flow and the heat transfer are driven by free convection, the increase of the buoyancy forces contributes to the heat transfer in the heat exchanger positively, and consequently, result in a faster phase change of the PCM.

The effect of *Ra* on MVF during charging and discharging is illustrated in Fig. 11. In discharging mode, the PCM is initially in the liquid phase. Shortly after, at $\tau = 0.052$, the PCM starts to solidify near the tube. A larger solid zone is observed for lower ε. As time goes, the solidification of the PCM continues. For $\varepsilon = 1$, the solid zone remains limited to the region near the tubes, while it ~~is~~ starting to spread throughout the cavity in the other two cases. At $\tau = 0.518$, the solid PCM covers the whole cavity for $\varepsilon = 0.9$, most of the cavity for $\varepsilon = 0.95$, but

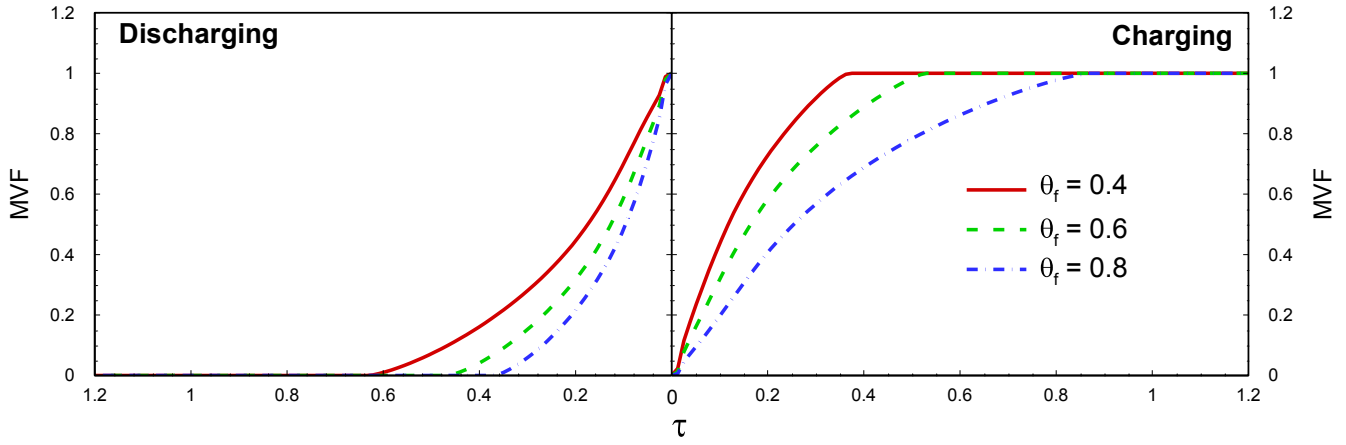

(a): $\varepsilon = 0.90$

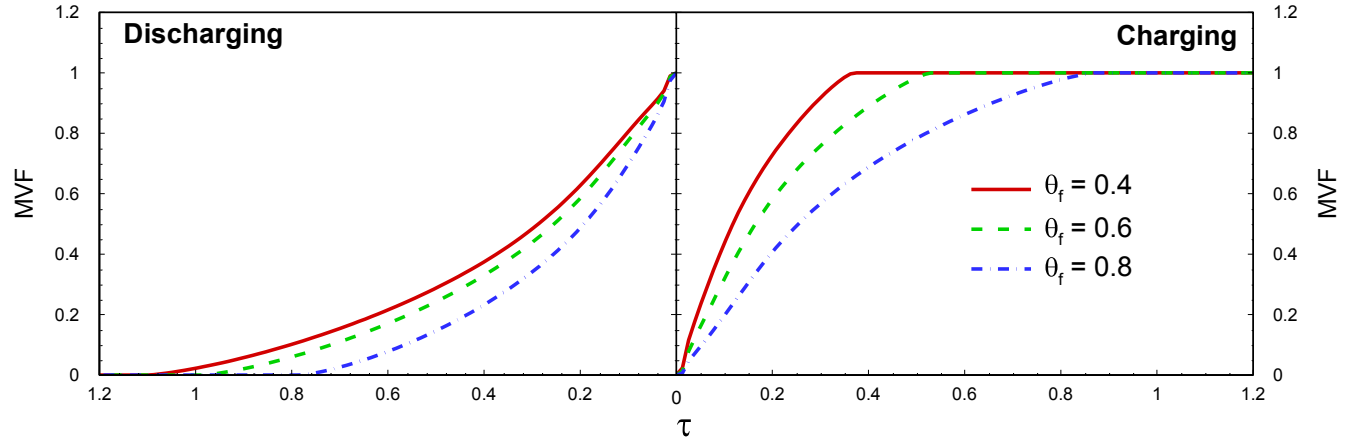

(b): $\varepsilon = 0.95$

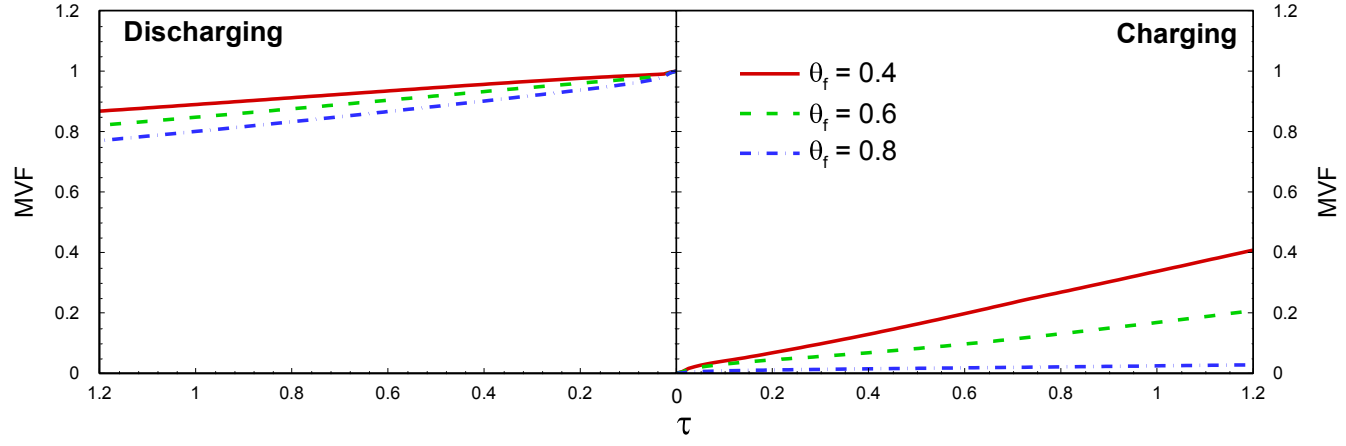

(c): $\varepsilon \approx 1.00$

Fig. 15. Melting volume fraction variation against dimensionless time for three different melting temperatures.

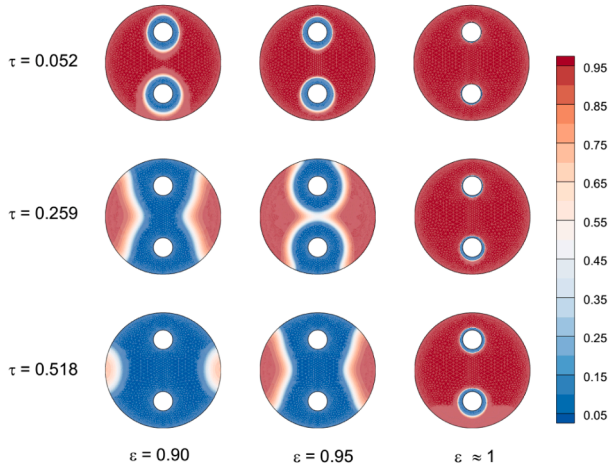

(a): $\theta_f = 0.4$

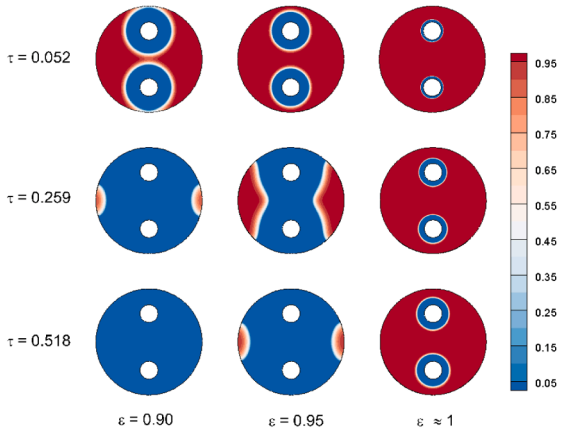

(b): $\theta_f = 0.8$

Fig. 16. Discharging state of melting volume fraction rate in different values of porosity and dimensionless melting temperature.

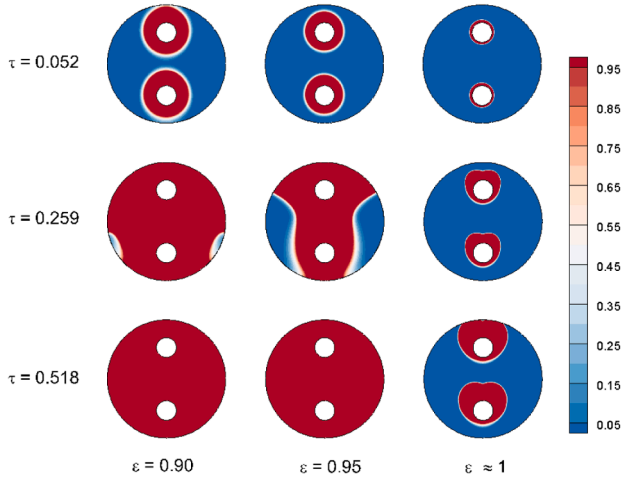

(a): $\theta_f = 0.4$

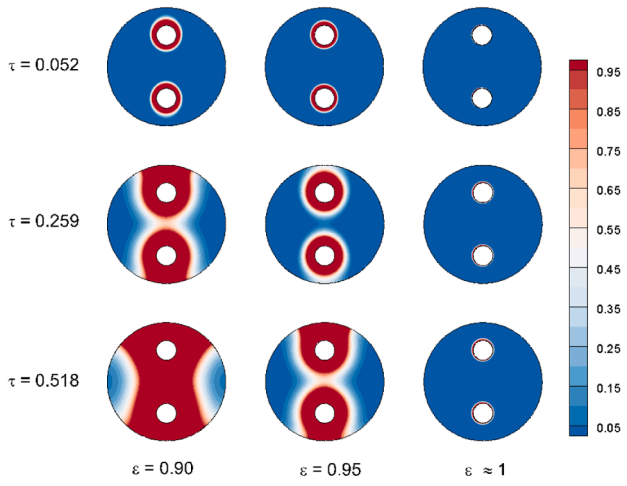

(b): $\theta_f = 0.8$

Fig. 17. Charging state of melting volume fraction rate in different values of porosity and dimensionless melting temperature.

stays limited to a small region around the tube for $\varepsilon = 1$, due to the absence of the solid matrix of copper enabling the temperature variation to spread in the PCM. The same behavior is observed in the charging mode when the PCM is melting. Starting from the solid phase, the PCM starts to melt near the tube, and full melting is promptly achieved for $\varepsilon = 0.9$, while the PCM remains in the solid phase except in a small region around the hot tube for $\varepsilon = 1$.

Figures 12 and 13 depict the location of the phase change interface during discharging for different values of ε during discharging and charging modes, respectively. In discharging mode, the solidification interface starts in a location near the cooling tube. As time goes, the depth of the solidification starts to increase, and the greatest depth is found for $\varepsilon = 0.95$. For $\varepsilon = 1$, the interface remains close to the tube. In a similar way, the melting interface remains close to the hot tube for $\varepsilon = 1$ in the charging mode. Besides, the furthest interface to the tube is observed for $\varepsilon = 0.9$. These observations confirm the result discussed in Fig. 11.

The isothermal contours during charge and discharge are shown in Fig. 14 for various values of ε. In discharging mode, for $\varepsilon = 0.9$, the isotherms for $\theta < 0.3$ are almost circular and surrounding the tube at $\tau = 0.207$. As τ reaches 0.388, the PCM cools down, and these isotherms move further towards the external shell. The isotherms corresponding to higher temperatures are concentrated near the external shell. A similar behavior but with denser isotherms is observed for $\varepsilon = 0.95$.

Nonetheless, for $\varepsilon = 1$, the isotherms are concentrated in the middle near the tube, indicating a thermal transfer limited to that region. The discrepancy between the cases $\varepsilon = 0.9$ and $\varepsilon = 0.95$ on one side and the case $\varepsilon = 1$ on the other is also apparent during charging. In the latter case, the isotherms corresponding to high temperatures are concentrated near the hot tube, i.e., in the only region where heat transfer is occurring. In the cases $\varepsilon = 0.9$, the high-temperature isotherms start near the hot tube then spread towards the external shell. When ε is increased to 0.95, the isotherms also start near the hot wall then move further towards the external shell, but remain limited to the middle of the cavity, indicating that the thermal transfer is slower than the case $\varepsilon = 0.9$.

Figure 15 illustrates the MVF as a function of time for a range of the melting temperature θ_f and various porosity (ε) during charging and discharging. The charging mode shows that the MVF is higher when θ_f is decreased and that the melting rate increases for lower melting temperatures. The fastest melting is achieved for $\theta_f = 0.4$. On the other side, during discharging, a faster solidification is obtained when θ_f is increased, and the zero value of the MVF is first attained for $\theta_f = 0.8$. This behavior is related to the definition of θ_f and the shift between θ_f

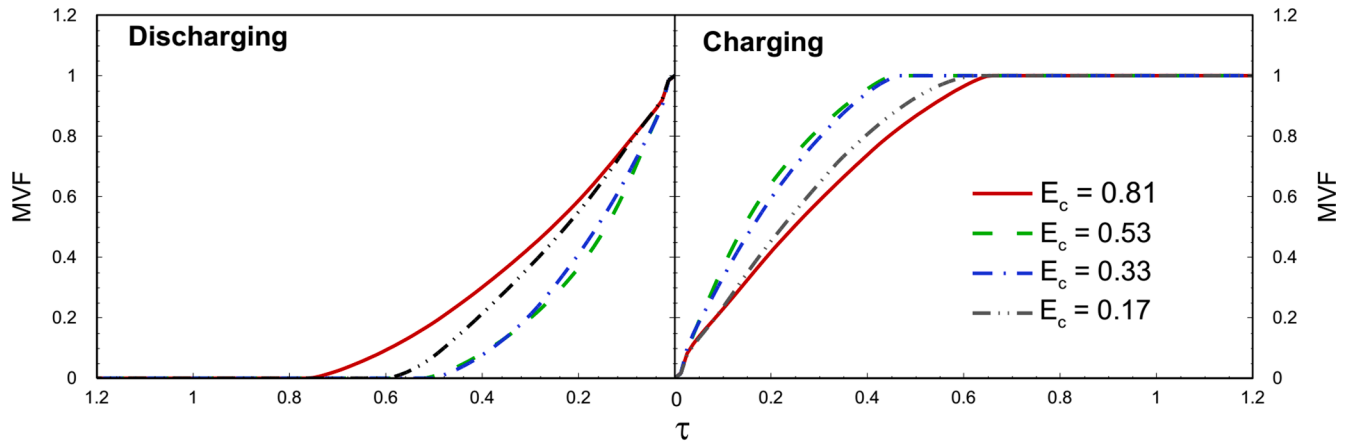

(a): $\varepsilon = 0.90$

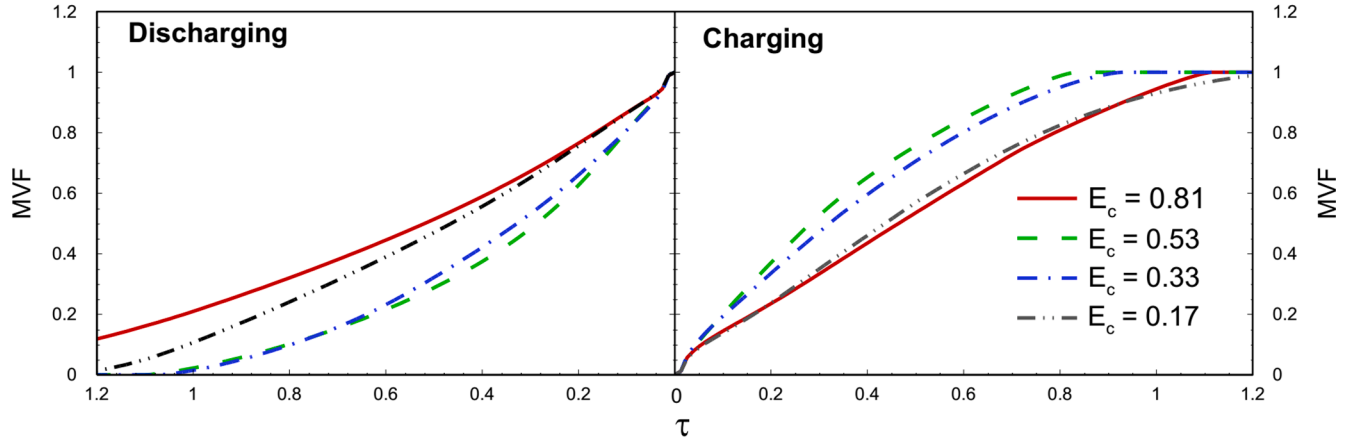

(b): $\varepsilon = 0.95$

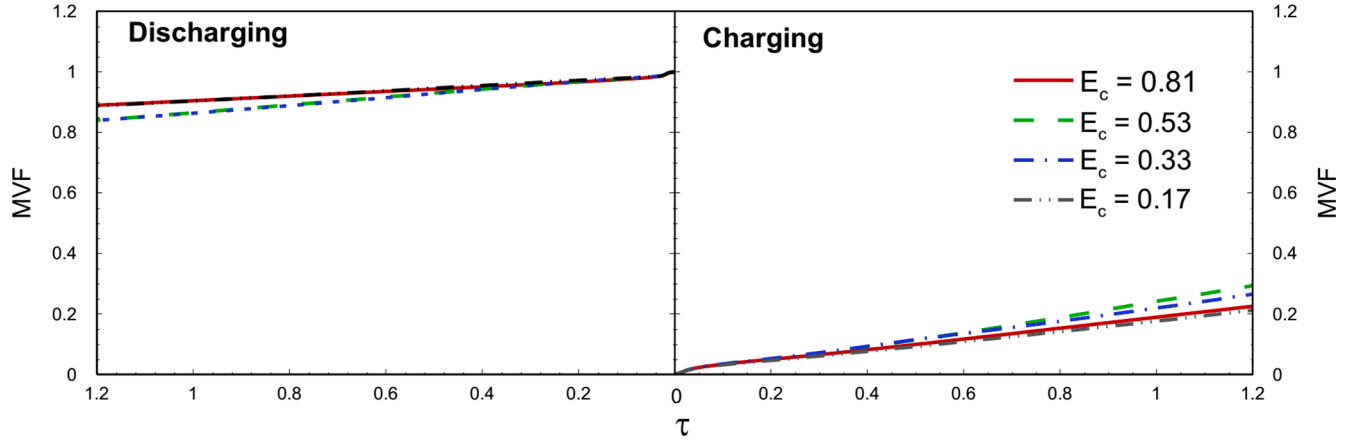

(c): $\varepsilon \approx 1.00$

Fig. 18. Melting volume fraction variation for different heat pipe positions.

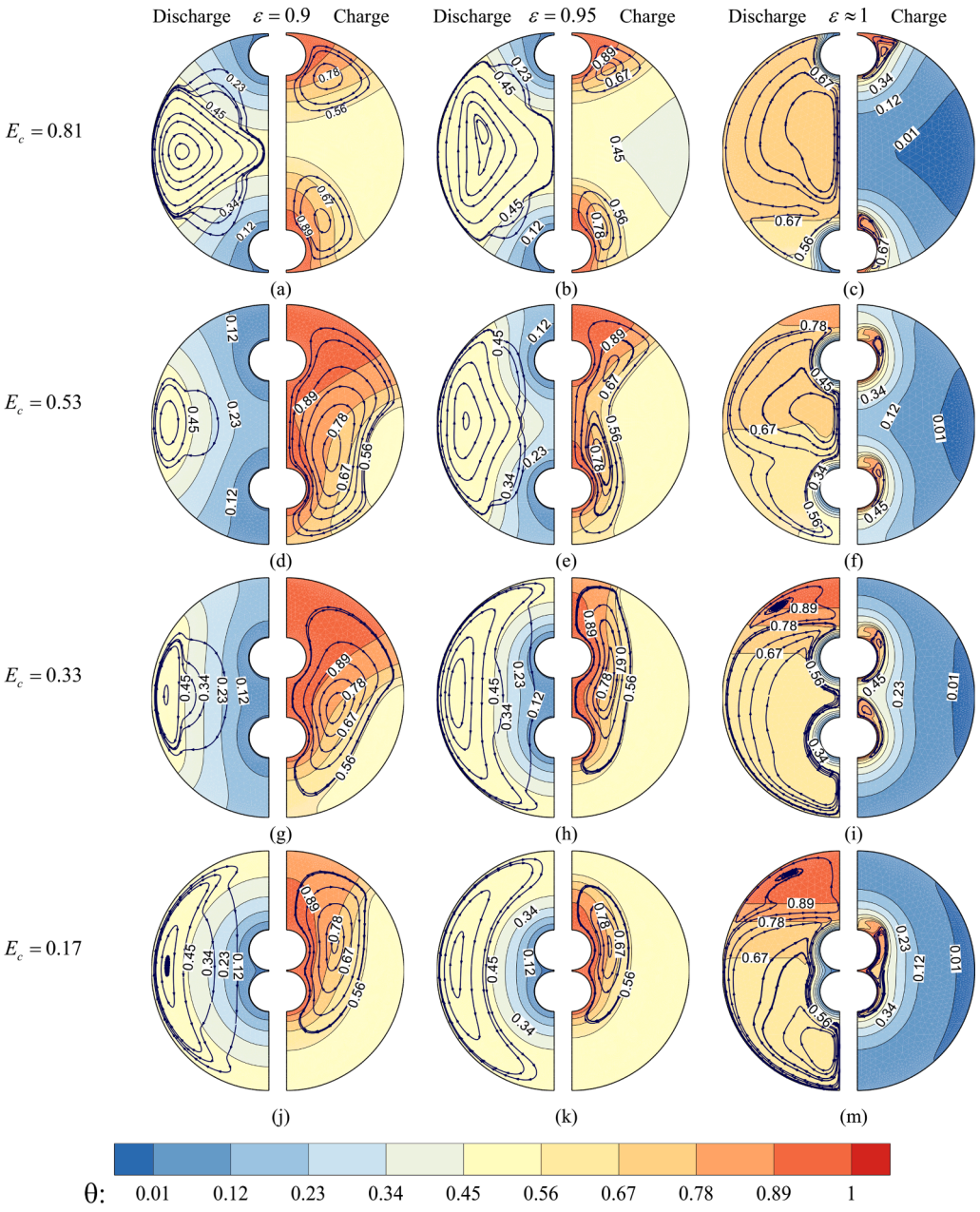

Fig. 19. Dimensionless temperature contours in different heat pipe positions at τ = 0.388.

and the tube temperature. In fact, the PCM is in the liquid state when the temperature in the region is $\theta > \theta_f$ and in the solid phase otherwise. During charging, the temperature of the tube is $\theta = 1$ so that the lower θ_f *is,* the greater the zone of melted PCM will be. Conversely, during discharging, the temperature of the tube is $\theta = 0$, and, thus, more PCM will solidify when a higher θ_f is used.

Figure 16 illustrates the time evolution of the MVF during discharging for different values of the melting temperature θ_f and ε. Comparing the cases (a) and (b) shows that since the initial stages, the size of the solid PCM is greater for $\theta_f = 0.8$, regardless of porosity values. This difference is barely apparent for $\varepsilon = 1$, where the solid PCM remains near the tube for the two values of θ_f. For the other two values of ε, it is observed that full solidification is achieved faster for $\theta_f = 0.8$. As mentioned, this is due to the discrepancy between θ_f and the tube's temperature during charging and discharging. The variation of MVF with time in charging mode is shown in Fig. 17 for various values of θ_f and ε. In the charging mode, the behavior of the melting PCM is opposite to the solidification behavior discussed in Fig. 16. In fact, the zone of melting PCM is in all cases higher for $\theta_f = 0.4$. Moreover, at this melting temperature, full melting is reached faster for $\varepsilon = 0.9$ and $\varepsilon = 0.95$.

Figure 18 illustrates the effect of the distance E_c between the upper and lower pipes on the variation of MVF with time for different values of ε. It can be seen that in charging mode, for all the values of ε, the MVF is at its highest value for $E_c = 0.53$, then for $E_c = 0.33$, and that the full melting is first achieved for this value. The MVF is at its lowest value for $E_c = 0.81$, where it is slightly lower than the case $E_c = 0.17$. The full melting is the slowest for these two values. Similarly, in the discharging mode, the fastest solidification is obtained for $E_c = 0.53$ and $E_c = 0.33$, while the slowest one is obtained for $E_c = 0.17$ and $E_c = 0.81$. The effect of E_c on MVF is less apparent for $\varepsilon = 1$, as a slight difference can be found in the value of MVF for the various values of E_c. These results indicate that bringing the upside and downside tubes too close or too far from each other negatively affects the rate of phase change of the PCM in the cavity.

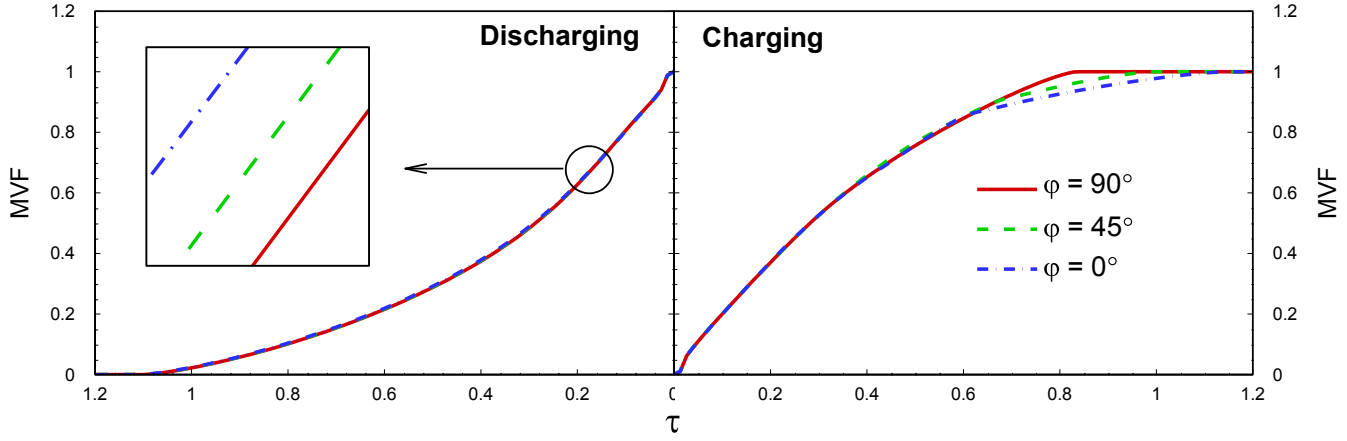

Fig. 20. The effect of tube orientations on melting volume fraction in both charging and discharging mode.

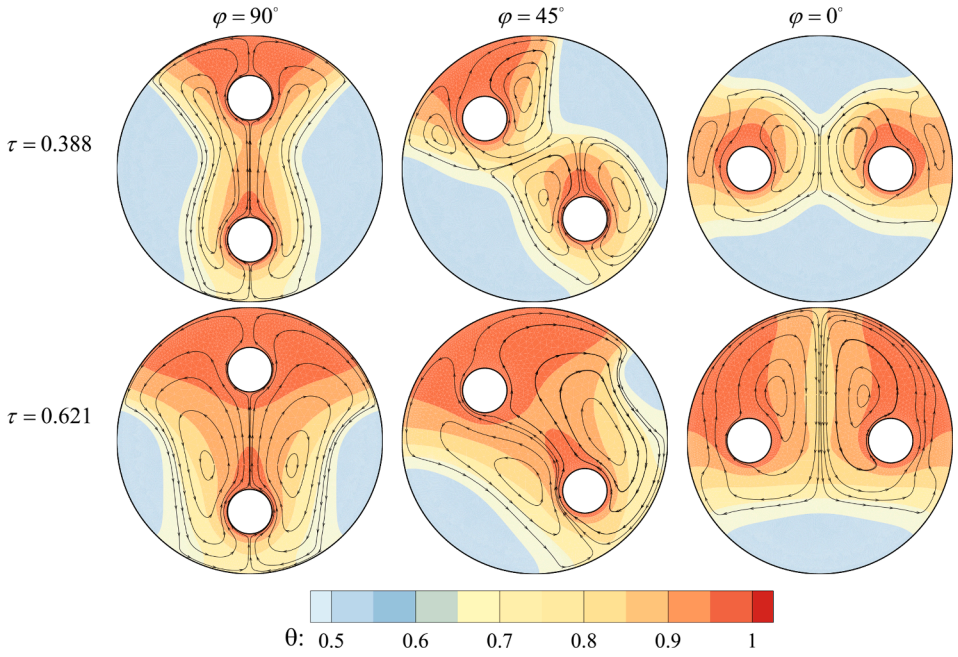

Fig. 21. . The effect of tube orientations (φ) on temperature distribution in charging mode.

The isotherms for different values of E_c during charging and discharging are depicted in Fig. 19 to illustrate better the effect of E_c on the thermal behavior in the exchanger. It is clear that varying the distance between the upside and downside pipes disturbs the isothermal contours. During charging, for $\varepsilon = 0.9$, it can be seen that for $E_c = 0.81$, the isotherms of high temperatures are limited to the zone near each tube and are not present in the area between the two tubes. Reducing the distance between the tubes, decreasing E_c to 0.17, limits the hot isotherms to the region around the two tubes, as if there is one tube in the center of the exchanger. For $E_c = 0.53$ and $E_c = 0.33$, the high-temperature isotherms are covering the hot tubes and the space between them. Similar behavior can be observed for $\varepsilon = 0.95$. On the other hand, for $\varepsilon = 1$, the isotherms corresponding to high temperature remain concentrated near the tubes for all the values of E_c. Thus, the variation of distance between tubes induces minimal impact on the heat transfer rate and melting behavior as long as these regions are separated. The same can be observed regarding the cold isotherms in discharging mode for the different values of ε. For $\varepsilon = 0.9$ and $\varepsilon = 0.95$, a high increase of the distance between the upper and lower tubes limits the cold isotherms to the zone near the tubes and restricts their development in the region between the tubes. Getting the two tubes too close to each other is similar to having one tube at the center and hinders the advantage of having two tubes in the exchanger.

Figure 20 shows the effect of the tube orientations (φ) on *MVF*. According to this figure, tubes with a 90-degree orientation are fully charged around $\tau = 0.8$, wherein the $MVF = 1$. However, tubes with 45° and 0° orientations need more time to be charged than the first status. From Fig. 20 can be concluded that the position of the tubes has no significant effect on the solidification process. Figs. 21 and 22 shows the temperature distribution in the investigated structures with different tube orientations. In charging mode (Fig. 21), the temperature profile and streamlines have a symmetrical pattern in the cavity when the tubes are located in the 90° and 0°. In 45° orientation, these uniform patterns do not exist. In this case, the temperature increases more rapidly in the structures with the 90° and 0° tube orientations. In contrast to the charging mode, the temperature profile and streamlines have a symmetrical pattern regardless of the tube orientations in discharging mode (Fig. 22).

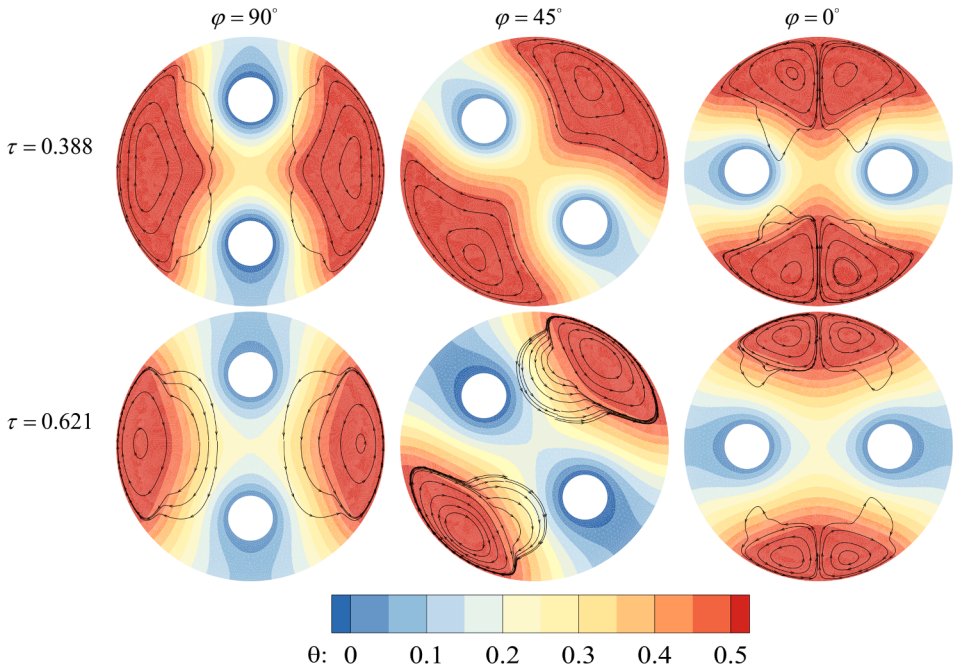

Fig. 22. . The effect of tube orientations (φ) on temperature distribution in discharging mode.

5. Conclusion

The flow and heat transfer of paraffin-embedded in copper foam was modeled using the enthalpy-porosity approach. The model equations were solved numerically using the FEM. The mesh adaptation technique and automatic time step control schemes were employed to track the melting interface with a high-resolution mesh and proper time steps. The results of the current numerical were compared with the experimental data in the literature and found in good agreement. The melting and solidification processes were investigated in a shell and tube thermal energy storage filled with the copper metal foam. The impact of Rayleigh number, metal foam porosity, and non-dimensional melting temperature on the phase change behavior of paraffin wax was explored. The key outcomes of the present computational analysis are summarized as follows:

- Filling the heat exchanger with copper foam and paraffin as a PCM increases the melting rate in the charging mode and the solidification rate in the discharging mode compared to the case with pure PCM due to the increased thermal conductivity. Decreasing the foam's porosity further contributes to the rise of the phase change rate in the two modes due to the increased size of the solid matrix and, consequently, of the thermal conductivity.
- The phase-change temperature (θ_f) could control the sizes of phase change zones by changing the temperature differences between the tube walls and the phase change interface. The relative distance between the upper and lower tubes in the exchanger is another important factor in the charging/discharging process. When the tubes are close to each other, the phase change regions around the tubes reach together and merge quickly. By placing the tubes too close, the temperature gradient drop in the region between the tube, and thus, the overall heat transfer reduces. When the tubes are with a fair distance, they do not impact the temperature gradients around each other and the merging of the melted regions takes place at the early stages of phase change. Thus, the tubes can boost the convection flows and accelerate the phase change. When the tubes are far from each other, the merging of phase change regions around the tubes takes place late, which reduces the charging/discharging rate ultimately.
- The rate of phase change during charging or discharging is increased when a higher value of Rayleigh number Ra is utilized. Raising the value of Ra indicates augmentation of the relative importance of buoyancy forces, and thus the free convection heat transfer is enhanced. The phase change of the PCM occurs faster as a result.
- The orientation of tubes does not affect the discharging time and MVF behavior. However, it shows influences on the final charging stages, where the melting advances to 80% and more. A vertical arrangement of tubes leads to the best charging time.

CRediT authorship contribution statement

Ali Veismoradi: Visualization, Formal analysis, Data curation, Software, Validation. **Mohammad Ghalambaz:** Conceptualization, Methodology, Software, Validation, Formal analysis, Data curation, Supervision, Writing - original draft, Writing - review & editing. **Hassan Shirivand:** Methodology, Writing - review & editing, Investigation, Validation, Software. **Ahmad Hajjar:** Methodology, Writing - original draft, Writing - review & editing, Investigation, Software. **Abdulmajeed Mohamad:** Conceptualization, Writing - review & editing. **Mikhail Sheremet:** Methodology, Writing - original draft, Writing - review & editing. **Ali Chamkha:** Methodology, Writing - original draft, Writing - review & editing. **Obai Younis:** Methodology, Writing - original draft, Writing - review & editing.

Declaration of Competing Interest

The authors declare that they have no known competing financial interests or personal relationships that could have appeared to influence the work reported in this paper.

Acknowledgement

This work of Mikhail Sheremet was conducted as a government task of the Ministry of Science and Higher Education of the Russian Federation (Project Number 0721-2020-0036).

References

[1] S.-F. Li, Z.-H. Liu, X.-J. Wang, A comprehensive review on positive cold energy storage technologies and applications in air conditioning with phase change materials, Appl. Energy 255 (2019) 113667.

[2] K. Faraj, M. Khaled, J. Faraj, F. Hachem, C. Castelain, Phase change material thermal energy storage systems for cooling applications in buildings: a review, Renew. Sustain. Energy Rev. 119 (2020) 109579.

[3] P.J. Shamberger, N.M. Bruno, Review of metallic phase change materials for high heat flux transient thermal management applications, Appl. Energy 258 (2020) 113955.

[4] B. Anupam, U.C. Sahoo, P. Rath, Phase change materials for pavement applications: a review, Constr. Build. Mater. 247 (2020) 118553.

[5] W. Su, J. Darkwa, G. Kokogiannakis, Numerical thermal evaluation of laminated binary microencapsulated phase change material drywall systems, in: Building Simulation, vol. 13, Springer, 2020, pp. 89-98.

[6] B. Gürel, A numerical investigation of the melting heat transfer characteristics of phase change materials in different plate heat exchanger (latent heat thermal energy storage) systems, Int. J. Heat Mass Transf. 148 (2020) 119117.

[7] M. Alizadeh, K. Hosseinzadeh, M. Shahavi, D. Ganji, Solidification acceleration in a triplex-tube latent heat thermal energy storage system using V-shaped fin and nano-enhanced phase change material, Appl. Therm. Eng. 163 (2019) 114436.

[8] M.K. Koukou, M.G. Vrachopoulos, N.S. Tachos, G. Dogkas, K. Lymperis, V. Stathopoulos, Experimental and computational investigation of a latent heat energy storage system with a staggered heat exchanger for various phase change materials, Therm. Sci. Eng. Progr. 7 (2018) 87–98.

[9] S. Park, S. Woo, J. Shon, K. Lee, Experimental study on heat storage system using phase-change material in a diesel engine, Energy 119 (2017) 1108–1118.

[10] S. Tiari, S. Qiu, M. Mahdavi, Discharging process of a finned heat pipe–assisted thermal energy storage system with high temperature phase change material, Energy Convers. Manage. 118 (2016) 426–437.

[11] Z. He, Q. Wan, Z. Wang, J. Zhang, S. Yi, The numerical simulation and experimental study of heat release in a heat storage system with various diameters of aluminum tubes, Heliyon 5 (2019) e02651.

[12] D. Guerraiche, C. Bougriou, K. Guerraiche, L. Valenzuela, Z. Driss, Experimental and numerical study of a solar collector using phase change material as heat storage, J. Storage Mater. 27 (2020) 101133.

[13] Z. Badiei, M. Eslami, K. Jafarpur, Performance improvements in solar flat plate collectors by integrating with phase change materials and fins: a CFD modeling, Energy 192 (2020) 116719.

[14] S. Hoseinzadeh, S.T. Otaghsara, M.Z. Khatir, P.S. Heyns, Numerical investigation of thermal pulsating alumina/water nanofluid flow over three different cross-sectional channel, Int. J. Numer. Meth. Heat Fluid Flow (2019).

[15] S. Hoseinzadeh, P.S. Heyns, H. Kariman, Numerical investigation of heat transfer of laminar and turbulent pulsating Al2O3/water nanofluid flow, Int. J. Numer. Meth. Heat Fluid Flow (2019).

[16] S. Hoseinzadeh, S. Sahebi, R. Ghasemiasl, A. Majidian, Experimental analysis to improving thermosyphon (TPCT) thermal efficiency using nanoparticles/based fluids (water), Eur. Phys. J. Plus 132 (2017) 197.

[17] R. Ghasemiasl, S. Hoseinzadeh, M. Javadi, Numerical analysis of energy storage systems using two phase-change materials with nanoparticles, J. Thermophys. Heat Transfer 32 (2018) 440–448.

[18] J. Darkwa, O. Su, Thermal simulation of composite high conductivity laminated microencapsulated phase change material (MEPCM) board, Appl. Energy 95 (2012) 246–252.

[19] J. Darkwa, O. Su, T. Zhou, Development of non-deform micro-encapsulated phase change energy storage tablets, Appl. Energy 98 (2012) 441–447.

[20] W. Su, J. Darkwa, G. Kokogiannakis, Review of solid–liquid phase change materials and their encapsulation technologies, Renew. Sustain. Energy Rev. 48 (2015) 373–391.

[21] N.S. Bondareva, M.A. Sheremet, Conjugate heat transfer in the PCM-based heat storage system with finned copper profile: application in electronics cooling, Int. J. Heat Mass Transf. 124 (2018) 1275–1284.

[22] N.S. Bondareva, M.A. Sheremet, Effect of nano-sized heat transfer enhancers on PCM-based heat sink performance at various heat loads, Nanomaterials 10 (2020) 17.

[23] N.S. Bondareva, B. Buonomo, O. Manca, M.A. Sheremet, Heat transfer inside cooling system based on phase change material with alumina nanoparticles, Appl. Therm. Eng. 144 (2018) 972–981.

[24] N.S. Bondareva, B. Buonomo, O. Manca, M.A. Sheremet, Heat transfer performance of the finned nano-enhanced phase change material system under the inclination influence, Int. J. Heat Mass Transf. 135 (2019) 1063–1072.

[25] N.S. Bondareva, N.S. Gibanov, M.A. Sheremet, Computational study of heat transfer inside different PCMs enhanced by Al2O3 nanoparticles in a copper heat sink at high heat loads, Nanomaterials 10 (2020) 284.

[26] P.T. Sardari, R. Babaei-Mahani, D. Giddings, S. Yasseri, M. Moghimi, H. Bahai, Energy recovery from domestic radiators using a compact composite metal Foam/PCM latent heat storage, J. Cleaner Prod. 257 (2020) 120504.

[27] A. Shahsavar, A. Goodarzi, H.I. Mohammed, A. Shirneshan, P. Talebizadehsardari, Thermal performance evaluation of non-uniform fin array in a finned double-pipe latent heat storage system, Energy 193 (2020) 116800.

[28] Z. Li, A. Shahsavar, A.A. Al-Rashed, P. Talebizadehsardari, Effect of porous medium and nanoparticles presences in a counter-current triple-tube composite porous/nano-PCM system, Appl. Therm. Eng. 167 (2020) 114777.

[29] P.T. Sardari, D. Giddings, D. Grant, M. Gillott, G.S. Walker, Discharge of a composite metal foam/phase change material to air heat exchanger for a domestic thermal storage unit, Renew. Energy 148 (2020) 987–1001.

[30] A. Shahsavar, J. Khosravi, H.I. Mohammed, P. Talebizadehsardari, Performance evaluation of melting/solidification mechanism in a variable wave-length wavy channel double-tube latent heat storage system, J. Storage Mater. 27 (2020) 101063.

[31] P.T. Sardari, H.I. Mohammed, D. Giddings, M. Gillott, D. Grant, Numerical study of a multiple-segment metal foam-PCM latent heat storage unit: effect of porosity, pore density and location of heat source, Energy 189 (2019) 116108.

[32] J.M. Mahdi, H.I. Mohammed, E.T. Hashim, P. Talebizadehsardari, E.C. Nsofor, Solidification enhancement with multiple PCMs, cascaded metal foam and nanoparticles in the shell-and-tube energy storage system, Appl. Energy 257 (2020) 113993.

[33] B. Buonomo, H. Celik, D. Ercole, O. Manca, M. Mobedi, Numerical study on latent thermal energy storage systems with aluminum foam in local thermal equilibrium, Appl. Therm. Eng. 159 (2019) 113980.

[34] M. Karkri, A numerical investigation of the effects of metal foam characteristics and heating/cooling conditions on the phase change kinetic of phase change materials embedded in metal foam, J. Storage Mater. 26 (2019) 100985.

[35] X. Hu, F. Zhu, X. Gong, Experimental and numerical study on the thermal behavior of phase change material infiltrated in low porosity metal foam, J. Storage Mater. 26 (2019) 101005.

[36] C. Wang, M. Mobedi, A new formulation for nondimensionalization heat transfer of phase change in porous media: an example application to closed cell porous media, Int. J. Heat Mass Transf. 149 (2020) 119069.

[37] X. Xiao, P. Zhang, M. Li, Preparation and thermal characterization of paraffin/metal foam composite phase change material, Appl. Energy 112 (2013) 1357–1366.

[38] O. Mesalhy, K. Lafdi, A. Elgafy, K. Bowman, Numerical study for enhancing the thermal conductivity of phase change material (PCM) storage using high thermal conductivity porous matrix, Energy Convers. Manage. 46 (2005) 847–867.

[39] H. Zheng, C. Wang, Q. Liu, Z. Tian, X. Fan, Thermal performance of copper foam/paraffin composite phase change material, Energy Convers. Manage. 157 (2018) 372–381.

[40] Y. Tian, C.-Y. Zhao, A numerical investigation of heat transfer in phase change materials (PCMs) embedded in porous metals, Energy 36 (2011) 5539–5546.

[41] J.C. De Los Reyes, S. González Andrade, A combined BDF-semismooth Newton approach for time-dependent Bingham flow, Numer. Methods Partial Differential Equations 28 (2012) 834–860.

[42] O. Schenk, K. Gärtner, Solving unsymmetric sparse systems of linear equations with PARDISO, Future Generation Comput. Syst. 20 (2004) 475–487.

[43] P. Wriggers, Nonlinear finite element methods, Springer Science & Business Media, 2008.

[44] F. Verbosio, A. De Coninck, D. Kourounis, O. Schenk, Enhancing the scalability of selected inversion factorization algorithms in genomic prediction, J. Computational Sci. 22 (2017) 99–108.

[45] T. Kuehn, R. Goldstein, An experimental and theoretical study of natural convection in the annulus between horizontal concentric cylinders, J. Fluid Mech. 74 (1976) 695–719.

[46] O. Bertrand, B. Binet, H. Combeau, S. Couturier, Y. Delannoy, D. Gobin, M. Lacroix, P. Le Quéré, M. Médale, J. Mencinger, H. Sadat, G. Vieira, Melting driven by natural convection A comparison exercise: first results, Int. J. Therm. Sci. 38 (1999) 5–26.

[47] A. Brent, V.R. Voller, K. Reid, Enthalpy-porosity technique for modeling convection-diffusion phase change: application to the melting of a pure metal, Numer. Heat Transfer, Part A Appl. 13 (1988) 297–318.

[48] S. Kashani, A. Ranjbar, M. Abdollahzadeh, S. Sebti, Solidification of nano-enhanced phase change material (NEPCM) in a wavy cavity, Heat Mass Transf. 48 (2012) 1155–1166.

[49] C. Gau, R. Viskanta, Melting and solidification of a pure metal on a vertical wall, 1986.